Atmos. Chem. Phys. Discuss., doi:10.5194/acp-2016-1173, 2017
Manuscript under review for journal Atmos. Chem. Phys.
Published: 1 February 2017

Atmospheric Chemistry and Physics Discussions

Lidar ratios of stratospheric volcanic ash and sulfate aerosols retrieved from CALIOP measurements

Andrew T. Prata[1], Stuart A. Young[2], Steven T. Siems[1], and Michael J. Manton[1]

[1]School of Earth, Atmosphere and Environment, Monash University, Clayton, Victoria 3800, Australia.
[2]CSIRO Oceans and Atmosphere, Aspendale, Victoria 3195, Australia.

Correspondence to: Andrew T. Prata (andrew.prata@monash.edu)

Abstract. We apply a two-way transmittance constraint to nighttime CALIOP (Cloud-Aerosol Lidar with Orthogonal Polarization) observations of volcanic aerosol layers to retrieve estimates of the particulate lidar ratio (S_p) at 532 nm. This technique is applied to three volcanic eruption case studies that were found to have injected aerosols directly into the stratosphere. Numerous lidar observations permitted characterisation of the optical and geometric properties of the volcanic aerosol layers over a time period of 1–2 weeks. For the volcanic ash layers produced by the Puyehue-Cordón Caulle eruption (June 2011) we obtain mean and median particulate lidar ratios of 72 $\pm$ 14 sr and 70 sr, respectively. For the sulfates produced by Kasatochi (August 2008) and Sarychev Peak (June 2009), the mean of the retrieved lidar ratios were 68 $\pm$ 21 sr (median 62 sr) and 66 $\pm$ 15 sr (median 61 sr), respectively.

The layer-integrated volume depolarisation ratios (δ_v) observed for the Puyehue ash layers (δ_v = 0.28 $\pm$ 0.03) were much larger than those found for the sulfate layers produced by the Kasatochi (δ_v = 0.08 $\pm$ 0.03) and Sarychev (δ_v = 0.05 $\pm$ 0.04) eruptions. However, for the Sarychev layers we observe an exponential decay (e-folding time of 1 week) in δ_v with time from 0.25 to 0.05. The layer-integrated attenuated colour ratios for the Puyehue ash layers (χ' = 0.54 $\pm$ 0.07) were also larger than what was observed for the Kasatochi (χ' = 0.35 $\pm$ 0.07) and Sarychev (χ' = 0.32 $\pm$ 0.07) sulfate layers, indicating that the Puyehue ash layers were generally composed of larger particles. These observations are particularly relevant to the new stratospheric aerosol subtyping classification scheme, which has been incorporated into version 4 of the level 2 CALIPSO data products.

1 Introduction

Stratospheric volcanic aerosols are formed when explosive volcanic eruptions inject SO_2 gas and silicate (SiO_2) ash particles into the stratosphere. The volcanic SO_2 can subsequently convert to sulfate aerosols (radii from 0.1–1 μm) to form stratospheric aerosol clouds with their radiative effects persisting from weeks to years depending on the timing, location and amount of precursory SO_2 gas (Carn et al., 2016; Kremser et al., 2016). According to the observational record, stratospheric sulfates formed as a result of major volcanic eruptions can cause abrupt changes in global stratospheric aerosol optical depth (SAOD; Sato et al., 1993; Bourassa et al., 2012; Rieger et al., 2015). Following the eruption of Pinatubo (Philippines, 1991), this change in SAOD led to a warming of the stratosphere (Labitzke and McCormick, 1992) and cooling of the troposphere (Dutton and

Atmos. Chem. Phys. Discuss., doi:10.5194/acp-2016-1173, 2017
Manuscript under review for journal Atmos. Chem. Phys.
Published: 1 February 2017

Atmospheric Chemistry and Physics Discussions

Christy, 1992). Small-to-moderate eruptions also have the ability to perturb SAOD (Vernier et al., 2011) and the cumulative effect of enhanced volcanism over the previous decade may have induced a volcanic forcing large enough to temporarily slow global warming (Solomon et al., 2011; Ridley et al., 2014; Santer et al., 2014).

Volcanic ash particles, although more short-lived than sulfates, can cause localised shortwave heating (Gerstell et al., 1995), generate regional-scale temperature anomalies (Mass and Robock, 1982) and pose a serious threat to civil aviation (Prata, 2016). In a modelling study, Niemeier et al. (2009) found that the radiative heating due to stratospheric fine ash particles, released at high latitude (60°N), influenced the regional wind flow. They argued that the combination of weak local flow, a strong Coriolis force and thermal expansion of air due to volcanic ash radiative heating led to the generation of localised vortices. The study highlighted the importance of characterising the optical properties of volcanic ash, especially during the first few weeks of an eruption.

Satellite measurements allow us to determine how volcanic ash and sulfates (collectively referred to here as 'volcanic aerosols') interact with solar and terrestrial radiation. Since 2006, the CALIOP instrument aboard the Cloud-Aerosol Lidar and Infrared Pathfinder Satellite Observations (CALIPSO) satellite has been making global, vertically resolved, attenuated backscatter measurements of the Earth's atmosphere (Winker et al., 2010). CALIOP observations have been used to identify stratospheric volcanic sulfates (Carn et al., 2007; Thomason and Pitts, 2008) as well as volcanic ash in the troposphere (Prata and Prata, 2012; Winker et al., 2012; Prata et al., 2015) and stratosphere (Vernier et al., 2013; Kristiansen et al., 2015).

The lidar equation for elastic backscatter lidars, which governs the CALIOP return signal, includes both molecular and particulate components. While the molecular terms can be estimated or modelled from atmospheric data, we are left with two unknowns (particulate backscatter and extinction) and one equation. This problem is usually overcome, as in the Fernald algorithm (Fernald et al., 1972; Fernald, 1984) by employing an extinction-to-backscatter ratio, which is now commonly referred to as the 'lidar ratio'.

Previously reported observations of the volcanic ash lidar ratio vary. Ansmann et al. (2010) and Groß et al. (2012) reported values in the range from 44–60 sr (at 532 nm), based on observations of the Eyjafjallajökull ash clouds over Germany. Wang et al. (2008) report lidar ratios from 42–65 sr for fine ash/sulfate mixed aerosol layers produced by the 2001 and 2002 eruptions of Mt Etna. For sulfate-rich layers, the lidar ratio was determined to be ∼48 sr for Nabro (Sawamura et al., 2012), 55 ± 4 sr for Sarychev (O'Neill et al., 2012) and 65 ± 10 sr for Kasatochi (Hoffmann et al., 2010).

Since CALIOP is an elastic backscatter lidar, in most cases the lidar ratio must be chosen *a priori* in order to retrieve the extinction profile. Based on extensive ground-based sun photometer measurements taken from the Aerosol Robotic Network (AERONET; Holben et al., 1998), Omar et al. (2009) have defined six aerosol subtypes for use with CALIOP measurements in version 3 of the data products; clean continental, polluted continental, polluted dust, desert dust, clean marine and smoke. In the version 4 release there will also be a dusty marine aerosol type in the troposphere and there will be four stratospheric types. The CALIOP scene classification algorithm (SCA; Omar et al., 2009), uses optical layer properties, surface type and layer height information to identify CALIOP feature layers as one of the predefined aerosol subtypes. By assigning each aerosol subtype with a characteristic lidar ratio, the extinction profile can be retrieved from CALIOP data (Young and Vaughan, 2009).

Atmos. Chem. Phys. Discuss., doi:10.5194/acp-2016-1173, 2017
Manuscript under review for journal Atmos. Chem. Phys.
Published: 1 February 2017

Atmospheric Chemistry and Physics Discussions

While the lidar ratio must be assigned *a priori* in the majority of cases, under certain conditions, Fernald's equations can be used to determine S_p from CALIOP measurements. This occurs when the lidar ratio solution is constrained by an estimate of the two-way transmittance (Young, 1995). Reliable estimates of the two-way transmittance are possible when sufficient clear air exists above and below a lofted cloud/aerosol layer. The transmittance method has previously been applied to optically thin cirrus layers (Sassen and Cho, 1992; Young, 1995), desert dust (Omar et al., 2010) and smoke plumes (Cook et al., 1972).

Stratospheric volcanic ash and sulfate layers are often observed as semi-transparent, laminar features (e.g. Winker and Osborn, 1992a; Vernier et al., 2013). Moreover, the stratosphere is generally free of meteorological clouds, desert dust, biomass burning and continental aerosols; providing the necessary clear-air conditions. The CALIOP backscatter signal-to-noise ratio (SNR), however, is significantly degraded by sunlight during the day. Thus, nighttime observations are generally required to perform a constrained retrieval on stratospheric volcanic aerosols.

Recently it has been shown that sulfate layers can be identified in CALIOP profiles using collocated measurements of SO_2 gas (Carboni et al., 2016). Since CALIOP is insensitive to SO_2, the underlying assumption is that volcanic SO_2 gas and $SO_4{}^{2-}$ aerosols are generally collocated. This is a reasonable assumption for the eruptions considered in the present study. Clarisse et al. (2013) showed that sulfate aerosols were detectable from the very onset of the Sarychev Peak eruption and that the infrared SO_2 and H_2SO_4 signatures were collocated in space and time for the first month. Similarly, Karagulian et al. (2010) demonstrated that the Kasatochi SO_2 cloud was collocated with sulfates for more than one month after the eruption.

This study uses the transmittance method and the Fernald solutions to characterise and explore the variability of the lidar ratio for stratospheric volcanic ash and sulfate layers. We present CALIOP-derived lidar ratios for the ash layers produced by the 2011 Puyehue-Cordón Caulle (hereafter Puyehue) eruption and the sulfate layers produced by the Kasatochi and Sarychev Peak (hereafter Sarychev) eruptions in 2008 and 2009, respectively. We use independent, passive infrared detection from the Atmospheric Infrared Sounder (AIRS) to identify volcanic ash in CALIOP profiles following the method presented by Prata et al. (2015). We also extend this method to sulfates using SO_2 as a proxy for $SO_4{}^{2-}$.

2 Satellite data

2.1 AIRS

The AIRS instrument is a part of the Afternoon-train (A-train; Stephens et al., 2002) and is aboard the Aqua satellite in sun-synchronous orbit at 705 km altitude. The AIRS spectrometer disperses upwelling radiation across highly sensitive detector arrays, which results in 2378 spectral samples (nominal spectral resolution of $\lambda/\Delta\lambda$ = 1200). These high-spectral resolution measurements cover three infrared wavebands (3.74–4.61 µm, 6.20–8.22 µm and 8.8–15.4 µm; Aumann et al., 2003) and can be used to detect volcanic ash (Prata et al., 2015) and SO_2 (Hoffmann et al., 2014). An individual AIRS granule comprises 90 $\times$ 135 pixels (1800 km $\times$ 2700 km) with a spatial resolution of 13.5 $\times$ 13.5 km^2 at nadir.

The data products used in the present study are the level 1B geolocated and calibrated radiances version 5.0.23. Only channels suitable for retrievals were used to calculate brightness temperatures (i.e. with L2_ignore flag set to zero; see http://disc.sci.gsfc.nasa.gov/AIRS/documentation).

Atmos. Chem. Phys. Discuss., doi:10.5194/acp-2016-1173, 2017
Manuscript under review for journal Atmos. Chem. Phys.
Published: 1 February 2017

Atmospheric Chemistry and Physics Discussions

2.2 CALIOP

The CALIPSO satellite is also a member of the A-train and carries the CALIOP instrument as its primary payload (Winker et al., 2010). Following closely behind Aqua (∼73 s), the space-borne lidar measures elastically backscattered light at 532 and 1064 nm using a three-channel receiver subsystem (Hunt et al., 2009). The ratio of the backscatter measured at these wavelengths (i.e. the attenuated colour ratio) can be used to infer information about particle size (Liu et al., 2009). The 532 nm signal is also split into two linear polarisation states, which enable depolarisation measurements to distinguish between irregular (e.g. ash, ice, dust) and spherical (e.g. sulfates) particles.

The CALIOP level 1 version 4, 532 nm total attenuated backscatter profiles (L1-Standard-V4-00) were used to generate attenuated backscatter curtain plots. The vertical resolutions of the level 1 backscatter profiles are altitude dependent and are broken down into five range intervals. For the altitudes ranges shown here (0–20 km), the relevant vertical resolutions are 30 m and 60 m for the altitude ranges from -0.5 to 8.2 km and 8.2 to 20.2 km, respectively.

The level 2 aerosol layer product version 3 (L2_05kmALay) was used to report geometric and optical layer properties. (Version 4, level 2 data had not been released at the time of writing.) The vertical resolution was 60 m as all volcanic layer observations were within the 8.2–20.2 km altitude range interval. To ensure constrained conditions for the lidar ratio retrieval (i.e. clear air above and below a lofted layer with acceptable SNR), only stratospheric volcanic aerosol layers that had an extinction quality control flag equal to 1 and a horizontal averaging value of 5 km were included in the analysis. We note that the operational lidar ratio data (Final_532_Lidar_Ratio) were not used because we wanted to adjust the multiple scattering factor (η) in the lidar ratio retrieval presented in Sect. 3.2.

As in Winker et al. (2012), the layer-integrated volume depolarisation ratio (δ_v) and layer-integrated attenuated colour ratio (χ') are defined as

$$\delta_v = \frac{\int_{r_t}^{r_b} \beta'_{\perp}(r)dr}{\int_{r_t}^{r_b} \beta'_{\parallel}(r)dr} \tag{1}$$

and

$$\chi' = \frac{\int_{r_t}^{r_b} \beta'_{1064}(r)dr}{\int_{r_t}^{r_b} \beta'_{532}(r)dr}, \tag{2}$$

where r is the range from the lidar, r_t and r_b are the ranges from the lidar to layer-top and layer-base, respectively, $\beta'_{\perp}(r)$ and $\beta'_{\parallel}(r)$ are the 532 nm perpendicular and parallel components of the attenuated backscatter, respectively, and $\beta'_{532}(r)$ and $\beta'_{1064}(r)$ are the attenuated backscatter profiles measured at 532 and 1064 nm, respectively.

The integrated attenuated backscatter, γ'_p, and the effective two-way transmittance at 532 nm, T^2_e, were also taken from the level 2 layer products as they are required for the lidar ratio retrieval. The CALIOP level 2 profile products (L2_05kmAPro) were used to obtain the normalised, ozone-corrected, total attenuated backscatter coefficient, $\beta'_N(r)$, which is also required as input into the lidar ratio retrieval. The reason for calculating $\beta'_N(r)$ from the level 2 operational products is so that a new value for η that is more representative of volcanic ash/sulfates could be used in the lidar ratio retrieval.

Atmos. Chem. Phys. Discuss., doi:10.5194/acp-2016-1173, 2017
Manuscript under review for journal Atmos. Chem. Phys.
Published: 1 February 2017

Atmospheric Chemistry and Physics Discussions

3 Methods

3.1 Volcanic aerosol detection in CALIOP profiles

In order to identify sulfate layers in CALIOP profiles, we assume SO_2 is collocated with SO_4^{2-} and adopt the SO_2 Index (SI) defined in Hoffmann et al. (2014). The SI is defined as the difference between brightness temperatures measured at 7.1 µm and 7.3 µm and exploits the strong absorption signature of SO_2 at 7.3 µm. It is defined such that positive values indicate the presence of SO_2 in the atmosphere. For ash layer detection, we use the BTD algorithm defined in Prata et al. (2015). To be consistent with the terminology used in Hoffmann et al. (2014), the ash BTD algorithm is referred to hereafter as the Ash Index (AI). The AI is a 12-channel BTD algorithm designed to exploit the reverse absorption signature of volcanic ash from 10.4–11.7 µm and 8.8–9.2 µm. We note that Prata et al. (2015) also introduced a temperature threshold (T_h) to remove false detections due to variable surface emissivity over land; however, it became clear that CALIOP detections of weak ash layers were removed by this threshold condition and so it was relaxed for the present study. As with the SI, the AI is defined such that positive values indicate the presence of volcanic ash.

Ash and sulfate layers are identified in CALIOP profiles based on collocated AIRS pixel values of the AI and SI, respectively. The collocation is achieved by calculating the minimum distance between a given CALIOP profile and the centre of each AIRS pixel. For the Puyehue case study, this set of collocated AIRS pixels is scanned for an AI greater than or equal to 1 K and SI below 1 K. For the Kasatochi and Sarychev case studies, the algorithm requires a SI greater than or equal to 1 K and an AI below 1 K. We also note that CALIOP profiles located south of 65°S were removed from the Puyehue analysis as conditions over Antarctica during the Southern Hemisphere winter (June/July) are conducive to polar stratospheric cloud (PSC) formation (Pitts et al., 2009).

3.2 The Fernald solutions for CALIOP

In order to retrieve the particulate lidar ratio, S_p, we use the two-component Fernald lidar ratio solution (Fernald et al., 1972),

$$S_p = \frac{1 - T_e^2(r_t, r_b) T_m^{2\eta S_p / S_m}(r_t, r_b)}{2\eta \int_{r_t}^{r_b} \beta'_N(r) T_m^{2(\eta S_p / S_m - 1)}(r_t, r) dr}, \tag{3}$$

where r is the range from the lidar, r_t and r_b are the ranges from lidar to layer-top and -base, respectively, η is the multiple scattering factor, S_m is the molecular lidar ratio and $T_m^2(r_t, r)$ and $T_e^2(r_t, r)$ are the molecular and effective two-way transmittance profiles, respectively.

The effective two-way transmittance constraint, $T_e^2(r_t, r_b)$, is calculated by taking the ratio of the mean scattering ratio below layer-base and above layer-top (Vaughan et al., 2009). We only considered the top layer in a given profile so that measurements of $T_e^2(r_t, r_b)$ were not degraded by signal attenuation introduced by overlying cloud/aerosol layers.

The multiple scattering factor, η, by definition, varies from 0 to 1 (Platt, 1973). Single scattering is represented by $\eta = 1$ while lower values of η represent increased multiple scattering. In the CALIPSO level 2 version 3 datasets, η is set to 0.6 for all stratospheric features. However, we argue that this approximation may overestimate the effect of multiple scattering in the

Atmos. Chem. Phys. Discuss., doi:10.5194/acp-2016-1173, 2017
Manuscript under review for journal Atmos. Chem. Phys.
Published: 1 February 2017

Atmospheric Chemistry and Physics Discussions

Table 1. Mean and standard deviation of the geometric layer properties for the Kasatochi, Sarychev and Puyehue case studies.

Eruption	Number of layers	Layer-top (km)	Layer-base (km)	Layer-thickness (km)
Kasatochi	116	13.60 ± 1.99	12.59 ± 1.98	1.01 ± 0.43
Sarychev	146	13.73 ± 1.89	12.45 ± 1.73	1.40 ± 0.41
Puyehue	308	12.44 ± 0.82	10.65 ± 0.62	1.79 ± 0.54

volcanic aerosols layers considered here. Winker (2003) demonstrated that the value of η for aerosols was a strong function of geometric thickness. Essentially, as the geometric thickness of the aerosol layer is increased the value of η asymptotes towards unity (layers thicker than 500 m correspond to $\eta \geq 0.85$). Given that the mean geometric thickness of the Puyehue ash layers was 1.79 $\pm$ 0.54 km (Table 1), η was assumed to be 0.90 $\pm$ 0.05. Accordingly, this value was set higher than the multiple scattering factor used for the Eyjafjallajökull ash layers (0.85 $\pm$ 0.05; Winker et al., 2012), which were reported to have a mean geometric thicknesses of 0.75 km (Winker et al., 2012). The multiple scattering effects of volcanic sulfates are expected to be similar to that of spherical, fine mode, sulfurous aerosols; analogous to the polluted continental aerosol subtype defined in Omar et al. (2009). For the polluted continental class, multiple scattering is also expected to have a small effect on the retrieved lidar ratio (Young et al., 2008). Considering also that the mean thicknesses of the Kasatochi and Sarychev layers were 1.01 $\pm$ 0.43 km and 1.40 $\pm$ 0.41 km, respectively (Table 1), η was set to 0.95 $\pm$ 0.05 for sulfate aerosols.

The normalised, ozone-corrected, total attenuated backscatter profile, $\beta'_N(r)$, can be calculated from the level 2 operational products using Eq. (10) of Young and Vaughan (2009):

$$\beta'_N(r) = [\beta_m(r) + \beta_p(r)]\, T^2_m(r_t, r) T^2_e(r_t, r), \tag{4}$$

where $\beta_m(r)$ and $\beta_p(r)$ are the molecular and particulate backscatter profiles, respectively, and the transmittance profiles are defined as

$$T^2_m(r_t, r) = \exp\left[-2S_m \int_{r_t}^{r} \beta_m(r')dr'\right] \tag{5}$$

and

$$T^2_e(r_t, r) = \exp\left[-2\eta S_p \int_{r_t}^{r} \beta_p(r')dr'\right]. \tag{6}$$

Here $\beta'_N(r)$ is calculated from the operational values of S_p, η and $\beta_p(r)$ provided in the level 2 aerosol layer and profile products. As noted previously, the reason for calculating $\beta'_N(r)$ from the level 2 operational products is so that S_p can be re-calculated, via Eq. (3), using a new value for η that is more representative of volcanic ash or sulfates. We also compared the re-calculated lidar ratio against the operational lidar ratio using the operational value for η as a check on our method and found that the average difference was $\sim$1%.

The molecular backscatter profile, $\beta_m(r)$, is calculated from the Global Modelling and Assimilation Office (GMAO; Rienecker et al., 2008) meteorological data provided with the CALIPSO datasets, and S_m is the molecular lidar ratio. Note that the

Atmos. Chem. Phys. Discuss., doi:10.5194/acp-2016-1173, 2017
Manuscript under review for journal Atmos. Chem. Phys.
Published: 1 February 2017

Atmospheric Chemistry and Physics Discussions

molecular lidar ratio is generally assumed to be $8\pi/3$. However, the narrow bandwidth of CALIOP's optical filter means that it does not see all the scattered wavelengths near the central elastic wavelength. It also includes the molecular polarisability term giving an actual value at 532 nm of $S_m = 8.70447$ sr rather than $8\pi/3 \approx 8.37758$ sr.

3.2.1 An iterative solution for the particulate lidar ratio

Since Eq. (3) is transcendental, we apply an iterative solution to retrieve S_p (Fernald et al., 1972). In order to initialise Eq. (3), the solution to the single-component lidar equation (see Eq. (7) of Fernald et al. (1972)) is used to calculate an initial estimate of the lidar ratio;

$$S_p = \frac{1 - T_e^2(r_t, r_b)}{2\eta\gamma'_p}, \tag{7}$$

where

$$\gamma'_p = \int_{r_t}^{r_b} \beta_p(r) T_p^2(r_t, r) dr. \tag{8}$$

Here γ'_p is the particulate integrated attenuated backscatter, which is taken from the level 2 aerosol layer products. In the operational products, γ'_p is approximated using the clear-air trapezoid technique (Vaughan et al., 2005). The initial value of S_p, derived from Eq. (7), is then substituted into the right-hand side of Eq. (3) to calculate a refined estimate of S_p. The refined estimate is then compared with the previous value of S_p and the iteration continues until consecutive solutions converge to within a threshold of 0.01%. This refinement is necessary for tenuous aerosol layers where the molecular component of backscatter becomes significant (Young, 1995).

4 Case studies and results

4.1 Kasatochi

Activity at the Aleutian Island volcano, Kasatochi (52.18°N, 175.51°W) began over a period from 7–8 August 2008 (Waythomas et al., 2010) with SO_2 detectable in the atmosphere for at least a month (Krotkov et al., 2010). Using the SI, it was found that the Kasatochi signature was detectable in AIRS measurements until 28 August 2008. All of the available nighttime CALIOP and AIRS data from 8–28 August covering a geographic region from 30°N to 90°N to 180°W to 180°E were included in the present analysis. As seen in Fig. 1a, the SO_2 dispersion was extremely complex, with the SO_2 cloud being dispersed into the atmosphere over a period of ∼3 weeks until it became well-mixed and undetectable by AIRS. In total, 116 valid lidar ratio retrievals were made for the Kasatochi volcanic sulfate layers. The mean layer-top height and thickness of the Kasatochi layers were 13.60 ± 1.99 km and 1.01 ± 0.43 km, respectively. The mean depolarisation and colour ratios were 0.08 ± 0.03 and 0.35 ± 0.07, respectively, indicating observations of sulfate layers composed of small, spherical particles. The mean and standard deviation of the lidar ratios for the Kasatochi sulfate layers retrieved over a time period from 8–28 August were 68 ±

Atmos. Chem. Phys. Discuss., doi:10.5194/acp-2016-1173, 2017
Manuscript under review for journal Atmos. Chem. Phys.
Published: 1 February 2017

Atmospheric Chemistry and Physics Discussions

Table 2. Mean and standard deviation of the optical layer properties for the Kasatochi, Sarychev and Puyehue case studies. The symbols used for the particulate lidar ratio, volume depolarisation ratio and volume colour ratio are S_p, δ_v and χ', respectively.

Eruption	Number of layers	S_p (sr)	δ_v	χ'
Kasatochi	116	68.00 ± 20.61	0.08 ± 0.03	0.35 ± 0.07
Sarychev	146	65.96 ± 15.17	0.05 ± 0.04	0.33 ± 0.09
Puyehue	308	71.70 ± 13.74	0.29 ± 0.03	0.54 ± 0.08

21 sr (median of 62 sr). Figure 2 shows the respective distributions of the optical properties for each eruption case study. The layer-mean properties are given in Tables 1 and 2.

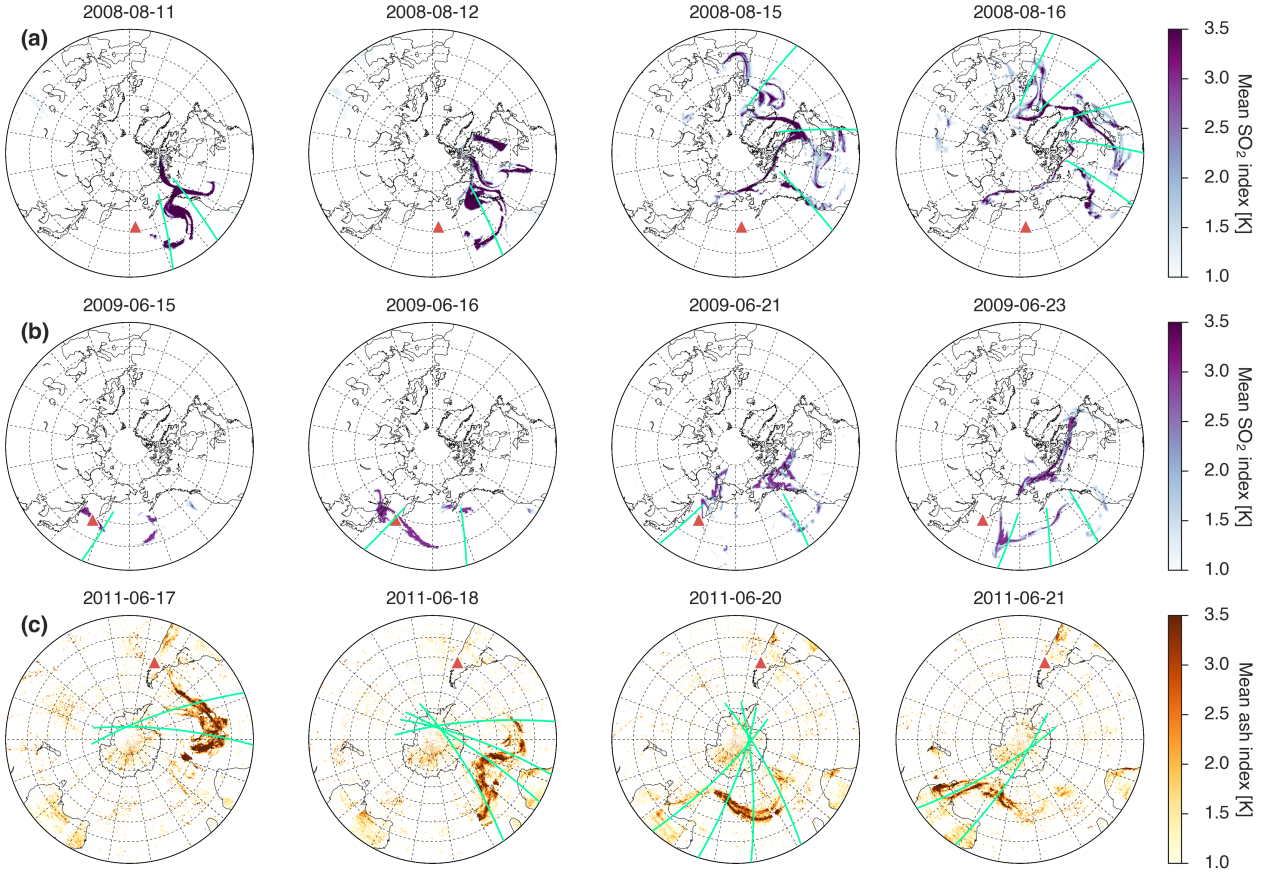

Figure 1. CALIOP/AIRS overview for a selected number of days for each of the case studies analysed; Kasatochi (a), Sarychev (b) and Puyehue (c). The locations of each volcano are plotted as red triangles. The AI (Ash Index) and SI (SO_2 Index) have been re-gridded into 0.5° × 0.5° grid boxes and have been averaged by the number of data points falling into a given grid box and therefore represent AI and SI means. Over-plotted green lines indicate CALIOP overpasses that contained valid lidar ratio retrievals.

Atmos. Chem. Phys. Discuss., doi:10.5194/acp-2016-1173, 2017
Manuscript under review for journal Atmos. Chem. Phys.
Published: 1 February 2017

Atmospheric Chemistry and Physics Discussions

4.2 Sarychev

Sarychev (48.09°N, 153.20°E), which is one of the most active volcanoes in the Kuril Island chain (Russia), began to erupt on 11 June 2009 (Rybin et al., 2011). AIRS detected an ash and SO_2 signature on June 12; however, CALIOP data was not available from 12–14 June 2009. According to surface observations, no more ash or SO_2 was seen emanating from the volcano after 24 June, but SO_2 was still detectable in the atmosphere (Williams and Thomas, 2011). Data for the Sarychev case study were therefore collected from 15 June to 12 July 2009, covering the same geographic region as the Kasatochi case study. Figure 1b provides an overview of the Sarychev SO_2 dispersion. Unlike Kasatochi, the Sarychev SO_2 signature initially separated into two distinct SO_2 clouds that dispersed toward the east and northwest. The eastward-traveling SO_2 cloud remained over the Alaskan peninsula for several days, while the northwestward SO_2 cloud travelled south as it crossed back over the volcano. In total, 146 valid lidar ratio retrievals were obtained. The optical properties of the Sarychev sulfate layers shared many similarities with the Kasatochi layers (Fig. 2). The mean depolarisation ratio was 0.05 ± 0.04 and mean colour ratio was 0.32 ± 0.07 (Table 2). The mean lidar ratio for the Sarychev layers was 66 ± 15 sr (median of 61 sr), corresponding to a layer-mean height and thickness of 13.73 ± 1.89 km and 1.40 ± 0.41 km, respectively (Table 1).

4.3 Puyehue

The eruption of Chilean volcano, Puyehue (40.59°S, 72.12 °W), was the first VEI 5 (Volcanic Explosivity Index; Newhall and Self, 1982) eruption since Cerro Hudson in 1991. The eruptions began on 4 June 2011 and resulted in wide-spread and far-reaching ash layers that caused flight cancellations in Australia and New Zealand. Vernier et al. (2013) analysed CALIOP observations of the Puyehue ash clouds and found the volcanic aerosol layers were primarily made up of ash particles and that sulfates contributed to less than 10% of the total attenuated backscatter. In the present analysis, we avoid ice-rich layers and identify ash-rich layers using passive infrared detection from collocated AIRS pixels (i.e. AI $\geq$ 1 K and SI < 1 K). The CALIPSO analysis presented by Vernier et al. (2013) also showed that the ash clouds remained near the tropopause as they were driven around the Southern Hemisphere by a strong westerly polar jet. This spatial description of the Puyehue ash clouds has been corroborated by several other authors (Klüser et al., 2013; Hoffmann et al., 2014; Theys et al., 2014).

CALIOP was switched into safe mode on 4 June, and again from 6–14 June 2011 (with 46.8% coverage on 15 June). During this time period the ash layers made their first circuit around the Southern Hemisphere. The observations included in the present analysis are therefore representative of aged (∼2 weeks) ash layers. The AIRS observations were analysed over a time period from 16 June to 4 July and a geographical area from 20°S to 90°S and 180°E to 180°W (Fig. 1c). The CALIOP profiles were restricted to latitudes north of or equal to 65°S to avoid PSCs (as noted in Sect. 3). In total, 308 valid lidar ratio retrievals were applied to CALIOP profiles containing stratospheric ash layers. The mean layer-top height and thickness of the Puyehue layers were 12.44 ± 0.82 km and 1.79 ± 0.54 km, respectively (Table 1). In contrast to Kasatochi and Sarychev, the Puyehue ash layers showed significant depolarisation ($\delta_v = 0.29 \pm 0.03$; Table 2), indicating non-spherical particles. The colour ratios of the Puyehue ash layers were also higher ($\chi' = 0.54 \pm 0.07$; Table 2) than the sulfates ($\chi' = 0.32$–0.35). The Puyehue lidar ratios (S_p mean of 72 ± 14 sr and median of 70 sr) were similar in magnitude to the sulfate lidar ratios of Kasatochi and Sarcyhev. The

Atmos. Chem. Phys. Discuss., doi:10.5194/acp-2016-1173, 2017
Manuscript under review for journal Atmos. Chem. Phys.
Published: 1 February 2017

Atmospheric Chemistry and Physics Discussions

lidar ratio distributions for the three case studies were similar in shape and were all positively skewed. We therefore provide both the mean and median lidar ratios (annotated on each histogram of Fig. 2).

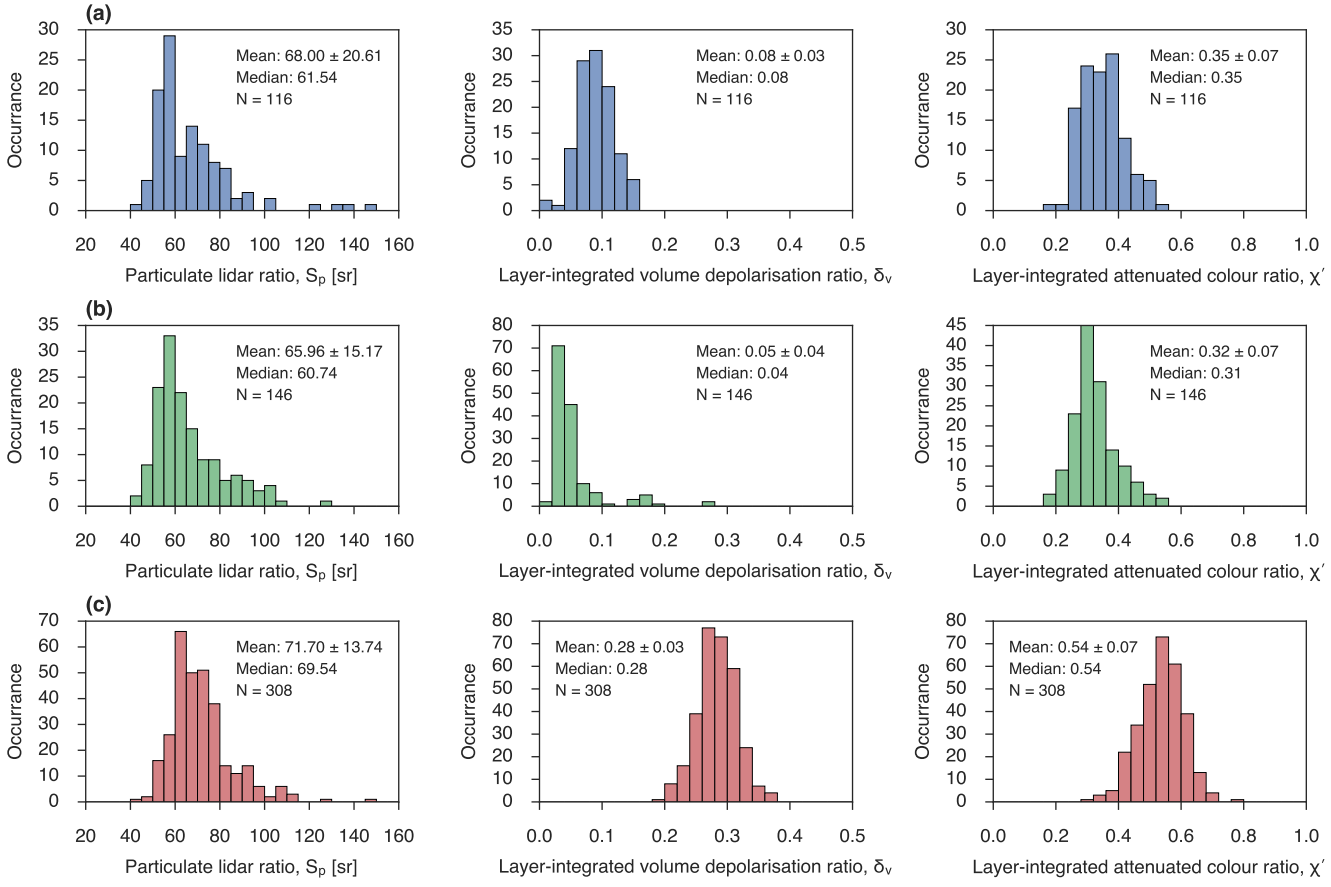

Figure 2. Histograms of the particulate lidar ratio (left column), layer-integrated volume depolarisation ratio (middle column) and layer-integrated attenuated colour ratio (right column) for the three case studies; (a) Kasatochi plotted in blue, (b) Sarychev plotted in green and (c) Puyehue in red.

5 Error sensitivity and propagation analysis

As discussed in Young et al. (2013), errors in a constrained retrieval of S_p can be broken down into two main categories: calibration/renormalisation error, $\epsilon(\beta'_N)$, and error in the transmittance constraint, $\epsilon(T_e^2)$. We also consider possible errors in the choice of the multiple scattering factor, $\epsilon(\eta)$. We do not, however, consider the impact of random noise on the lidar ratio retrieval. Essentially, we assume that error due to random noise will be negligibly small after 5 km averaging and thus insignificant in comparison to the other sources of error.

Atmos. Chem. Phys. Discuss., doi:10.5194/acp-2016-1173, 2017
Manuscript under review for journal Atmos. Chem. Phys.
Published: 1 February 2017

Atmospheric Chemistry and Physics Discussions

5.1 Errors in calibration/normalisation

Rogers et al. (2011) provide a comprehensive assessment of the version 3.01 CALIOP 532 nm total attenuated backscatter calibration. For nighttime measurements under clear-air conditions the mean relative error was reported to be 2.7% ± 2.1% when compared against airborne HSRL measurements. One of the main sources of error that is particularly relevant here, can arise in the case of an undetected (background) stratospheric aerosol layer. Vernier et al. (2009) highlighted how this issue would impact the CALIOP calibration region, concluding that undetected aerosols up to 35 km lead to an underestimation of the aerosol scattering ratio (an average relative error of 6%), with the effects most pronounced in the tropics (20°N–20°S). Although the observations presented here are confined to middle–high latitude regions, they directly coincide with ongoing volcanic eruption events, and so we must consider errors introduced by aerosol contamination (which have not been corrected for in the version 3 datasets).

Considering the ∼5% calibration error suggested by Rogers et al. (2011) and the 6% aerosol contamination error suggested by Vernier et al. (2009), we anticipated a relative error of 10% in the normalised, attenuated backscatter profile (i.e. $\epsilon(\beta'_N)/\beta'_N$ = 10%).

5.2 Errors in transmittance

The CALIOP level 2 aerosol products provide an estimate of the measured two-way transmittance error, which is calculated as the standard deviation of the attenuated scattering ratio in the clear air region below the detected layer (Vaughan et al., 2005). For the case studies considered, the means (and standard deviations) of the two-way transmittance relative errors were 15.91% ± 2.79%, 16.76% ± 2.72%, and 16.93% ± 4.08% for Kasatochi, Sarychev and Puyehue, respectively. However, since the operational algorithm (Vaughan et al., 2009) assumes pure Rayleigh scattering above the top layer of a given CALIOP profile, it is assumed that there is no attenuation by undetected layers aloft and that all of the attenuation is in the detected layer. In this case the estimate of T_e^2 will be too low and S_p will be too high. Rogers et al. (2011) considered the possible influence of volcanic aerosols affecting the two-way transmittance between 8–30 km. Based on volcanic stratospheric optical depths from Mattis et al. (2010), they estimated a maximum bias in the two-way transmittance of 3%. Considering the mean transmittance errors for the three case studies (∼17%) and the error introduced by undetected volcanic aerosols (∼3%), a relative error of 20% in the effective two-way transmittance constraint was assumed (i.e. $\epsilon(T_e^2)/T_e^2$ = 20%).

5.3 Error propagation analysis

To estimate how the errors in β'_N, T_e^2 and η propagate into errors in S_p a multi-variable functional approach (Hughes and Hase, 2010) was applied to Eq. (3) to calculate a perturbation error for each variable. As discussed in the previous sections, β'_N and T_e^2 were perturbed by 10% and 20%, respectively, and η was perturbed by 0.05. If any variable was perturbed outside of its physical bounds then it was set to the relevant upper or lower bound. Each perturbation error was then summed in quadrature to calculate the absolute error in the particulate lidar ratio:

$$\epsilon(S_p) = \pm\sqrt{\epsilon(S_{p,\beta'_N})^2 + \epsilon(S_{p,T_e^2})^2 + \epsilon(S_{p,\eta})^2}, \quad (9)$$

Atmos. Chem. Phys. Discuss., doi:10.5194/acp-2016-1173, 2017
Manuscript under review for journal Atmos. Chem. Phys.
Published: 1 February 2017

Atmospheric Chemistry and Physics Discussions

where $\epsilon(S_{p,\beta'_N})$, $\epsilon(S_{p,T_e^2})$ and $\epsilon(S_{p,\eta})$ represent the three components of error in S_p. The subscripts represent the variable that was perturbed while holding the other two variables constant. Figure 3 illustrates, for each case study, how each of the three perturbation errors propagated into the error in S_p. The assumed relative errors in β'_N and T_e^2, translated into mean absolute component errors of ∼6 sr and ∼14 sr, respectively, while the assumed error perturbations of 0.05 in η corresponded to errors in S_p of ∼3 sr. Overall, the perturbation errors, when summed in quadrature, corresponded to a mean absolute error in S_p of ∼15 sr.

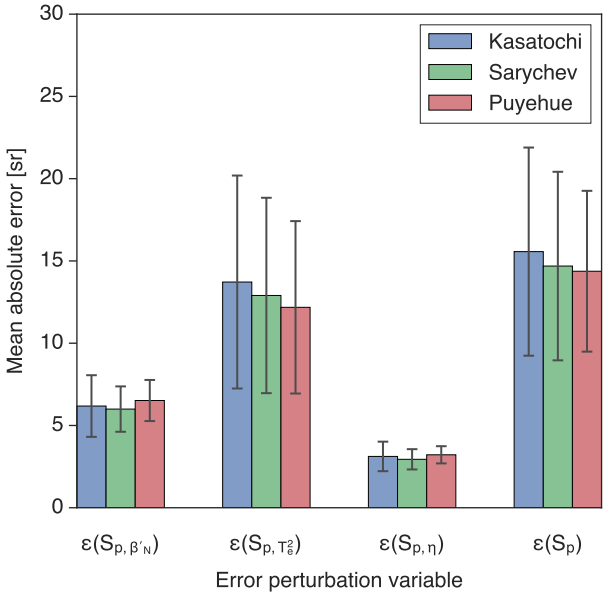

Figure 3. Perturbation errors for each case study; Kasatochi (blue), Sarychev (green) and Puyehue (red). The standard deviations for each perturbation error are plotted as whiskers over each bar plot.

As T_e^2 was considered to be the largest source of error in S_p, we examined how the relative error in the lidar ratio, $\epsilon(S_p)/S_p$, varied as a function of T_e^2 (Fig. 4). Here we see that the relative error in S_p asymptotes toward ∼10% as T_e^2 approaches zero and increases exponentially as T_e^2 approaches unity. In other words, for non-transmissive (optically thick) layers, error in the retrieved value of S_p will be limited by errors in β'_N and η. For highly transmissive (optically thin) layers, error in T_e^2 will become the dominant source of error in S_p.

Atmos. Chem. Phys. Discuss., doi:10.5194/acp-2016-1173, 2017
Manuscript under review for journal Atmos. Chem. Phys.
Published: 1 February 2017

Atmospheric Chemistry and Physics Discussions

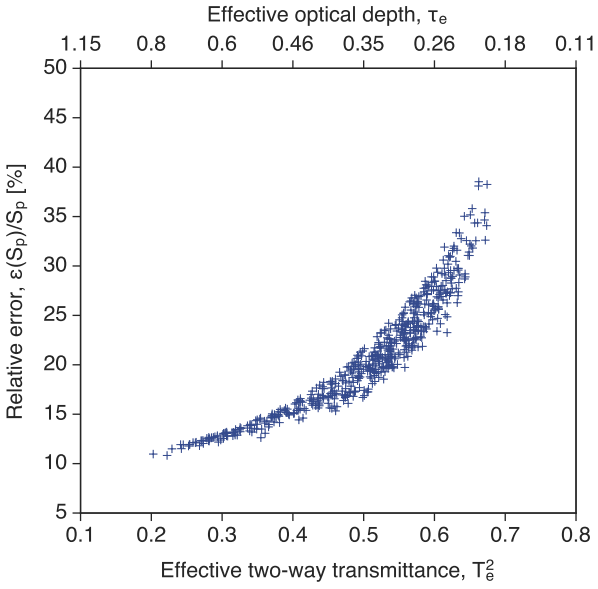

Figure 4. Relationship between T_e^2 and the relative error in the particulate lidar ratio, $\epsilon(S_p)/S_p$.

6 Discussion

6.1 Lidar ratio retrievals for selected observations

Figures 5–7 illustrate the CALIOP/AIRS analysis for an individual granule from each case study. For the Kasatochi and Sarychev sulfate layers (Fig. 5 and Fig. 6, respectively), the lidar ratio is relatively constant throughout the strongly backscattering regions of the stratospheric layers. The AIRS SO_2 signals also collocate well with the sulfate layers. The curtain-average value of the lidar ratio for the two-sulfate layers are also very similar ($S_p \sim 54$ sr). The mean volume depolarisation ratios for the sulfates are both relatively low ($\delta_v < 0.2$) indicating that these layers are dominated by spherical particles. The low mean depolarisation ratio ($\overline{\delta_v} = 0.04$) and strong SO_2 signature implies that the Sarychev layer is dominated by spherical sulfate particles. The attenuated colour ratios for the sulfate observations are also quite similar (χ' = 0.33–0.37) and indicate that these aerosol layers are made up of small particles.

The Puyehue ash layers (Fig. 7) are quite similar to the sulfate layers in terms of the geometric thickness; however, the layer-integrated optical properties, along with the AIRS ash signal, unambiguously identify this layer as being made up of non-spherical ash particles. The variability in the lidar ratio for the Puyehue observation generally increases as features become more tenuous, reflecting an increase in sensitivity in the lidar ratio retrieval for transmissive layers (as discussed in Sect. 5.3).

Atmos. Chem. Phys. Discuss., doi:10.5194/acp-2016-1173, 2017
Manuscript under review for journal Atmos. Chem. Phys.
Published: 1 February 2017

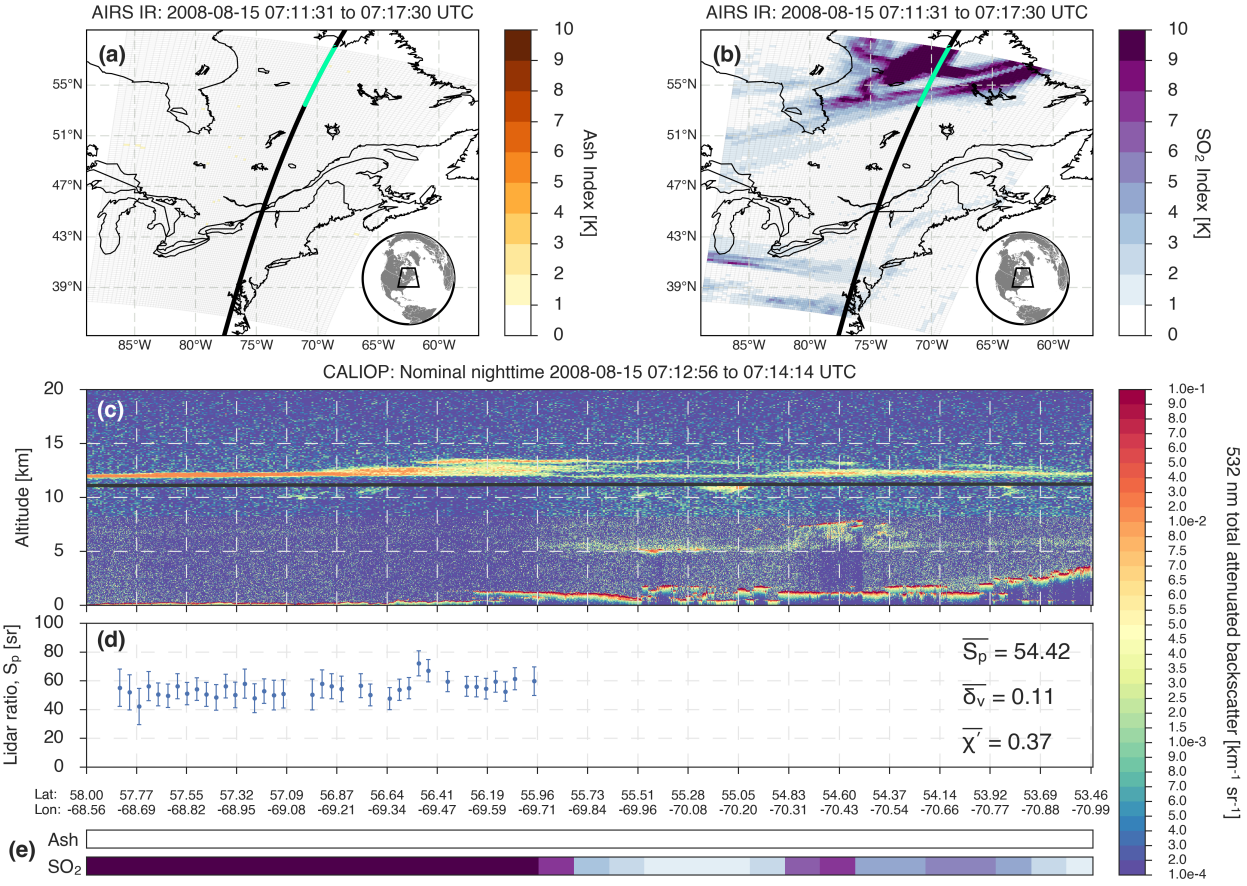

Figure 5. CALIOP/AIRS observations of a stratospheric volcanic sulfate layer produced by the 2008 Kasatochi eruption. (a) AIRS swath with the AI (Ash Index) plotted. The CALIOP trace (black line) is over-plotted and the section of the CALIOP trace corresponding to the CALIOP curtain panel, plotted in (c), is highlighted in green. (b) Same as (a) but for the SI (SO_2 Index). (c) CALIOP curtain plot (longitude/latitude vs. total attenuated backscatter) with the GMAO tropopause height over-plotted in black. (d) Particulate lidar lidar ratio retrievals (error bars are calculated from Eq. (9)). The curtain-mean values of the particulate lidar ratio ($\overline{S_p}$), layer-integrated depolarisation ratio ($\overline{\delta_v}$) and colour ratio ($\overline{\chi'}$) are annotated on the right-hand side of the plot. (e) AI and SI AIRS pixels that have been collocated along the CALIOP track.

Atmos. Chem. Phys. Discuss., doi:10.5194/acp-2016-1173, 2017
Manuscript under review for journal Atmos. Chem. Phys.
Published: 1 February 2017

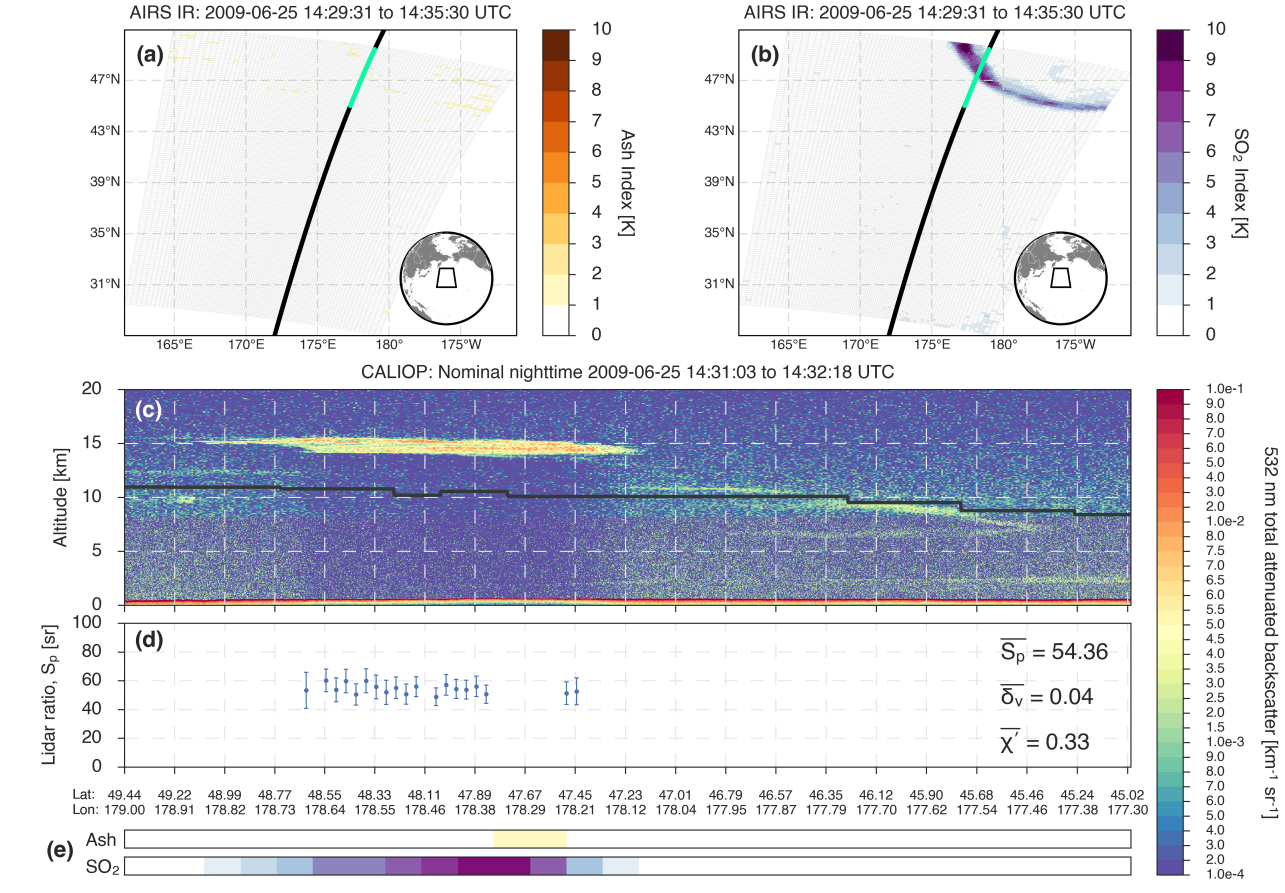

Figure 6. Same as Fig. 5 but for a stratospheric volcanic sulfate layer produced by the 2009 Sarychev eruption.

6.2 Time evolution of volcanic aerosol optical properties

As volcanic aerosol layers evolve and disperse into the atmosphere their microphysical properties are expected to change with time. The Kasatochi and Puyehue layers were observable for a duration of ∼5 days, while the Sarychev observations covered a time period of ∼12 days. Figure 8 shows that all observations were made more than three days after eruption onset. The Kasatochi observations are representative of the earlier stages of volcanic sulfate layer evolution and the Puyehue observations are more representative of long-range transported ash layers that resided in the stratosphere for more than 2 weeks. The Sarychev case study provided the longest observational time period of volcanic aerosol layer evolution of the three case studies considered.

The particulate lidar ratios for Kasatochi show a steady decrease with time from 75 sr to 55 sr over the first 4 days of observations, followed by an increase to 65 sr from day 7–8 (Fig. 8a). The lidar ratio observations were more variable with time for the Sarychev case study; however, when averaged over the total observation period the lidar ratios generally increased

Atmos. Chem. Phys. Discuss., doi:10.5194/acp-2016-1173, 2017
Manuscript under review for journal Atmos. Chem. Phys.
Published: 1 February 2017

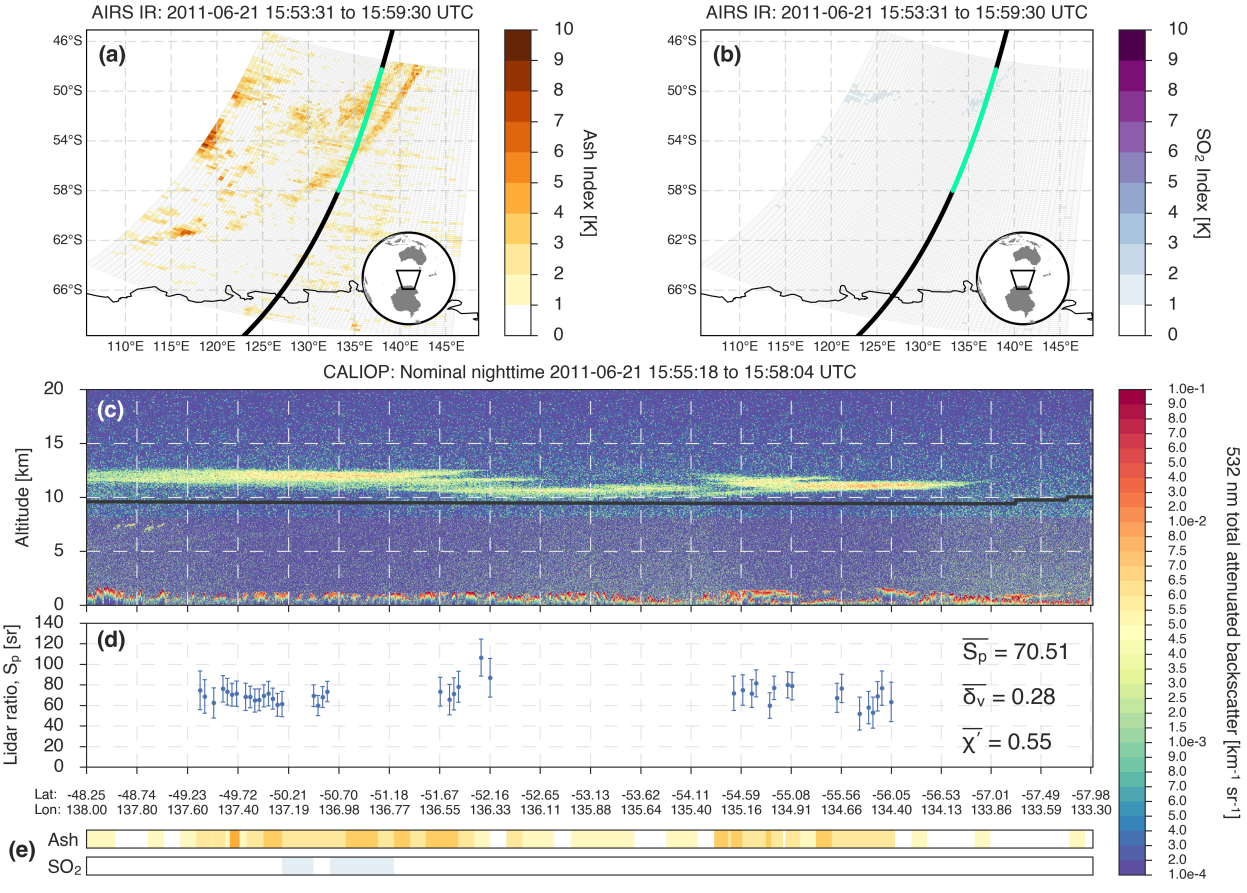

Figure 7. Same as Fig. 5 but for a stratospheric volcanic ash layer produced by the 2011 Puyehue eruption.

with time from 60 sr to 70 sr. The Puyehue lidar ratios were the least variable and exhibited a linear increase with time over ∼5 days from 65 to 70 sr.

The triangles corresponding to the right hand axis of Fig. 8a–c demonstrate how changes in S_p with time are inversely related to the integrated attenuated backscatter, γ'_p. As an SO_2-rich volcanic cloud develops, the integrated attenuated backscatter would be expected to initially increase as SO_2 molecules are oxidised and hydrated to form sulfate particles. Since the particulate lidar ratio is inversely proportional to backscatter, this process would lead to a reduction in S_p with time. On the other hand, as layers mature and particles fall out of the atmosphere due to sedimentation processes, γ'_p will decrease leading to an increase in S_p toward the later stages of layer development. For the ash-rich layers of Puyehue, it is likely that the increase in S_p with time is being driven by particle sedimentation processes (i.e. a decrease in γ'_p with time).

The Puyehue lidar ratios (65–70 sr) are relatively high in comparison to previously reported volcanic ash lidar ratios (40–60 sr; Ansmann et al., 2010; Groß et al., 2012). In fact, the Puyehue lidar ratios share interesting similarities with long-range transported Saharan desert dust lidar ratios (40–75 sr; Mattis et al., 2002). Mattis et al. (2002) provide two main reasons for

Atmos. Chem. Phys. Discuss., doi:10.5194/acp-2016-1173, 2017
Manuscript under review for journal Atmos. Chem. Phys.
Published: 1 February 2017

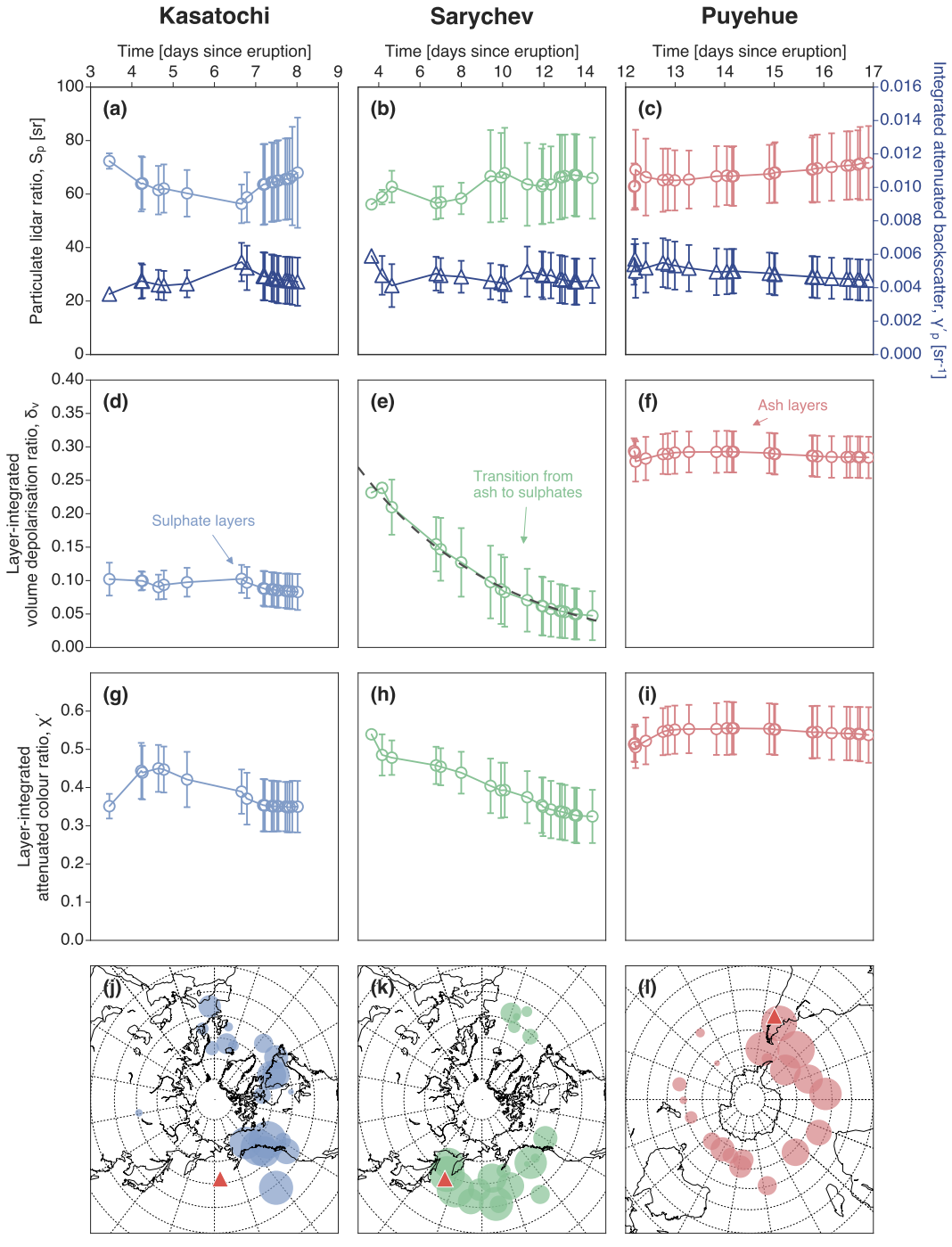

Figure 8. Time evolution of the optical properties for Kasatochi (left column), Sarychev (middle column) and Puyehue (right column). (a)–(c) Left axis corresponds to CALIOP curtain mean and standard deviation (error bars) of S_p (plotted as circles) and right axis corresponds γ'_p (plotted as triangles). (d)–(f) The same as (a)–(c) but for the layer-integrated volume depolarisation ratio (δ_v). Also plotted, on (e), is an exponential fit (black dashed line) corresponding to an e-folding time of 1 week. (g)–(i) The same as (a)–(c) but for the layer-integrated attenuated colour ratio (χ'). (j)–(l) Geographic representation of the data plotted on panels (a)–(i) with the size of the data points scaled to be negatively proportional to the residence time of the volcanic aerosol layers. Locations of volcanoes are plotted as red triangles.

Atmos. Chem. Phys. Discuss., doi:10.5194/acp-2016-1173, 2017
Manuscript under review for journal Atmos. Chem. Phys.
Published: 1 February 2017

Atmospheric Chemistry and Physics Discussions

high lidar ratios of long-range transported dust particles. The first is an increase in the fine to coarse mode particle ratio due to gravitational settling of coarse mode (diameters >1 μm) particles. The second is a large reduction in backscattering efficiency due to the non-sphericity of the particles. Both explanations are consistent with the Puyehue observations. The ash layers were observed after 12 days of long-range transport (providing the necessary time for coarse mode particles to fall out) and the layers were also dominated by irregular, highly depolarising ($\delta_v \sim 0.30$) particles.

The volume depolarisation ratios of the Puyehue ash layers were generally much larger than the Kasatochi and Sarychev layers (Figs. 8d–f). Note that δ_v is not strictly a particle property, but for layers dominated by aerosols it can be used as a first approximation to the particulate depolarisation ratio, δ_p (Wiegner et al., 2012). The Puyehue depolarisation ratios were higher than expected for aged (∼2 weeks) ash particles as there are few observations of aged ash layers with depolarisation ratios higher than 0.30 (e.g. Pinatubo; Winker and Osborn, 1992b). Ansmann et al. (2010), Groß et al. (2012) and Wiegner et al. (2012) reported particulate depolarisation ratios from 0.35–0.40 for Eyjafjallajökull ash observed over Germany; however, these were observations of young (1–3 days old) tropospheric ash layers.

Over the ∼2 weeks of Sarychev CALIOP observations, δ_v is seen to decay from 0.25 to 0.05 exponentially with time. This decay corresponds to an e-folding time of 1 week (dashed line; Fig 8e). Since the Sarychev layers were only analysed if the CALIOP observations were collocated with an AI < 1 K and SI $\geq$ 1 K, it is possible that the CALIOP instrument is detecting ash layers with a very weak reverse absorption signature that have not been removed by the AI threshold criterion. Papayannis et al. (2012) reported changes in depolarisation from 0.30 to 0.10 with time for the Eyjafjallajökull ash layers, suggesting humidity uptake (Lathem et al., 2011) as a mechanism for increasing the overall sphericity of the volcanic aerosols with time. Sulfate coating has also been offered as a mechanism for altering depolarisation with time (e.g. Povey et al., 2014). Humidity uptake is unlikely to explain the decay in δ_v for the Sarychev observations due to the lack of water vapour in the stratosphere. Also note that volume depolarisation will decease ($\delta_v \rightarrow \delta_m$) with time as the scattering ratio (ratio of total backscatter to molecular backscatter) decreases ($R \rightarrow 1$) even if the particulate depolarisation remains constant. The results presented here suggest that the earlier observations of the Sarychev layers contained irregular ash particles and as the layer evolved, SO_2 converted to sulfate, ash particles sedimented out and the layers became dominated by spherical (sulfate) particles.

This physical process might also explain the time evolution of the layer-integrated attenuated colour ratio, χ' (Figs. 8g–i). For the Sarychev layers an overall decrease in χ' is observed, suggesting a transition to smaller particles. Interestingly, the Kasatochi colour ratios show an initial increase, before gradually decreasing with time. This increase in χ' may indicate coagulation/condensation processes leading to particle growth at the earlier stages of layer development.

Overall, the Puyehue ash colour ratios reported here ($\chi' = 0.54 \pm 0.07$) are in agreement with the values reported by Vernier et al. (2013). These colour ratios are at the low end of values reported for the free-tropospheric ash layers produced by Eyjafjallajökull (0.47–0.77; Winker et al., 2012) and considering the high particulate lidar ratios ($S_p \sim 70$ sr) and significant depolarisation ratios ($\delta_v \sim 0.30$) these results suggest that the CALIOP observations of the Puyehue aerosol layers are representative of fine mode, ash particles. The Kasatochi ($\chi' = 0.35 \pm 0.07$) and Sarychev ($\chi' = 0.32 \pm 0.07$) colour ratios were, on average, quite similar but both were lower than those found for the Puyehue case study. This indicates that the Puyehue ash particles were larger than the Kasatochi and Sarychev sulfates. The sulfate colour ratios ($\chi' = 0.30$–0.35) were also lower than

Atmos. Chem. Phys. Discuss., doi:10.5194/acp-2016-1173, 2017
Manuscript under review for journal Atmos. Chem. Phys.
Published: 1 February 2017

Atmospheric Chemistry and Physics Discussions

typical colour ratios for desert dust ($\chi' \sim 0.45$; Liu et al., 2009), while the Puyehue ash colour ratios ($\chi' \sim 0.55$) were higher. Both classes of volcanic aerosols had smaller colour ratios than those CALIOP typically observes for ice (χ' = 0.7–1.2) and water clouds (χ' = 1–1.4; Hu et al., 2009).

6.3 Discriminating properties of CALIOP layer-products

Figure 9a compares the optical properties of the Kasatochi and Sarychev sulfates with the Puyehue ash retrievals. When combined, the depolarisation ratio and colour ratio plots emphasise distinctive differences between the two classes of volcanic aerosol. These optical properties are relevant to the new stratospheric aerosol classification scheme that considers δ_v, χ' and γ'_p (Tackett et al., 2016). The results of the present analysis are in support of a sub-classification scheme, also suggested by O'Neill et al. (2012) that categorises stratospheric sulfate layers having volume depolarisation ratios of $0 < \delta_v \leq 0.2$ (Fig. 9a; dashed line). Further classification could potentially be achieved using the colour ratios (e.g. $\chi' \leq 0.4$ = sulfates, $0.4 < \chi' \leq 0.7$ = ash). However, distinctions between ash and sulfates using χ' are less obvious than distinctions made with δ_v.

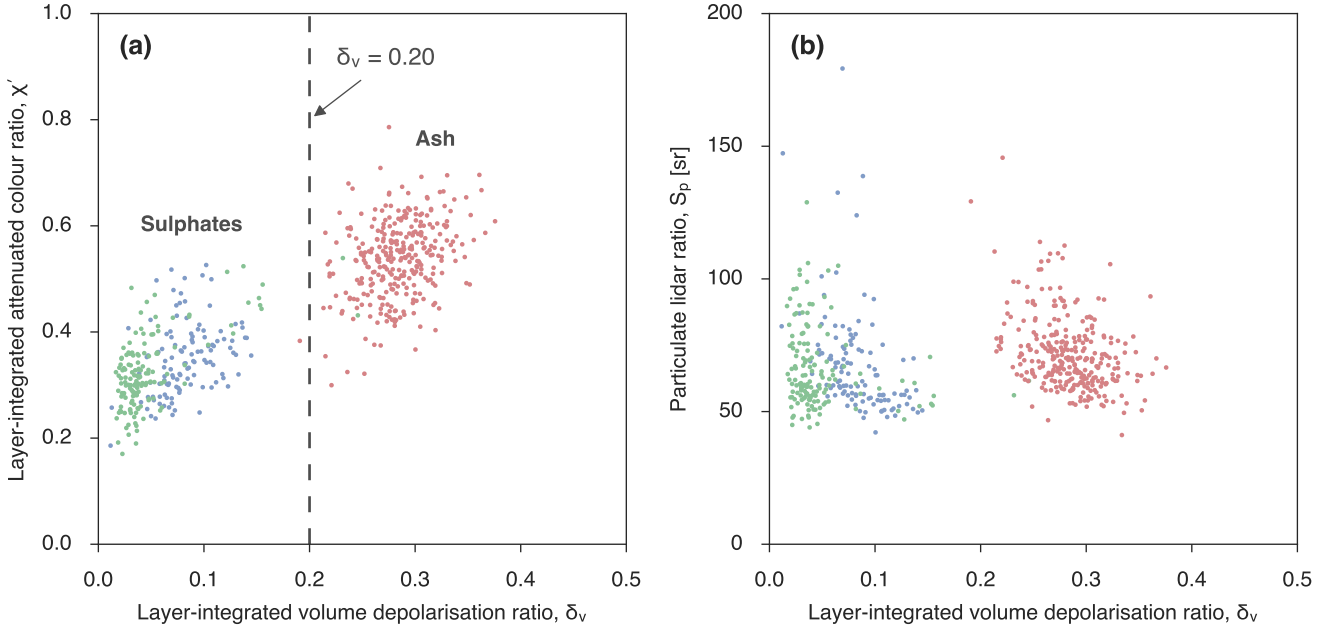

Figure 9. Optical properties of the Kasatochi (blue), Sarychev (green) and Puyehue (red) volcanic aerosols. (a) The relationship between the layer-integrated volume depolarisation ratio and the layer-integrated attenuated colour ratio. (b) The relationship between the particulate lidar ratio and the layer-integrated volume depolarisation ratio.

Figure 9b shows the relationship between the particulate lidar ratio and the volume depolarisation ratio. As previously noted, the particulate lidar ratios for the Puyehue ash and the sulfates of Kasatochi and Sarychev were similar. This would make it difficult to discriminate between ash and sulfates using S_p alone. Nevertheless, these lidar ratio retrievals provide important

Atmos. Chem. Phys. Discuss., doi:10.5194/acp-2016-1173, 2017
Manuscript under review for journal Atmos. Chem. Phys.
Published: 1 February 2017

Atmospheric Chemistry and Physics Discussions

Table 3. Mean, median and standard deviation of the particulate lidar ratio for different values of the multiple scattering factor for the Kasatochi, Sarychev and Puyehue case studies.

	Kasatochi S_p (sr)			Sarychev S_p (sr)			Puyehue S_p (sr)		
Multiple scattering factor, η	Mean	Median	Std. Dev.	Mean	Median	Std. Dev.	Mean	Median	Std. Dev.
0.50	121.41	112.58	27.18	120.75	111.99	26.92	123.46	119.71	22.71
0.55	112.61	103.30	29.69	109.77	101.81	24.47	112.24	108.83	20.64
0.60	103.22	94.69	27.22	100.63	93.33	22.43	102.9	99.76	18.92
0.65	95.47	87.55	25.15	93.14	86.47	20.77	95.27	92.45	17.51
0.70	90.28	81.72	26.97	86.99	80.70	19.50	89.17	86.59	16.50
0.75	84.64	76.58	25.35	81.66	75.70	18.40	83.93	81.47	15.66
0.80	79.70	72.09	23.94	77.00	71.25	17.44	79.34	76.98	14.94
0.85	75.34	68.12	22.70	72.89	67.24	16.59	75.29	73.09	14.30
0.90	71.47	64.65	21.60	69.23	63.73	15.84	71.70	69.54	13.74
0.95	68.00	61.54	20.61	65.96	60.74	15.17	68.48	66.45	13.23
1.00	64.88	58.74	19.72	63.02	58.10	14.57	65.58	63.46	12.78

information for distinguishing volcanic aerosols from water ($S_p \approx 20$ sr) and ice ($S_p \approx 25$ sr) clouds and could potentially be utilised in new lidar aerosol classification schemes (e.g. Groß et al., 2014).

6.4 Multiple scattering considerations

In order to facilitate interpretation of the results presented in Sect. 4, η was held constant for each case study. However, since the 'true' value of η for volcanic aerosols is unknown we provide S_p calculated for a range of different η values in Table 3. The relationship between η and S_p for the three case studies is also shown in Fig. 10. As expected from Eq. (7), the mean particulate lidar ratio decreased as the assumed multiple scattering factor was increased.

Previously reported values of the lidar ratio (at 532 nm) provide insight into the likely range of S_p for case studies considered here. The reported lidar ratios (at 532 nm) for Kasatochi and Sarychev range from 40–65 sr (Mattis et al., 2010). Although it is difficult to make direct comparisons (due to a lack of coincident observations), these values support a choice of η closer to unity for sulfates.

To our knowledge there have been no lidar ratio observations reported in the scientific literature for the Puyehue ash layers. However, ground-based lidar observations were made at Lauder, New Zealand. Nakamae et al. (2014) applied the Fernald (1984) algorithm to ground-based lidar measurements to derive aerosol (particulate) extinction profiles. They assumed a lidar ratio of 50 sr, but noted better agreement with independently derived optical depths when they set S_p to 60 sr. Their initial choice of lidar ratio was based on previous reports of the lidar ratio for the Eyjafjallajökull ash layers. According to Fig. 10, a lidar ratio of 60 sr corresponds to a multiple scattering factor close to unity (Fig. 10).

Atmos. Chem. Phys. Discuss., doi:10.5194/acp-2016-1173, 2017
Manuscript under review for journal Atmos. Chem. Phys.
Published: 1 February 2017

Atmospheric Chemistry and Physics Discussions

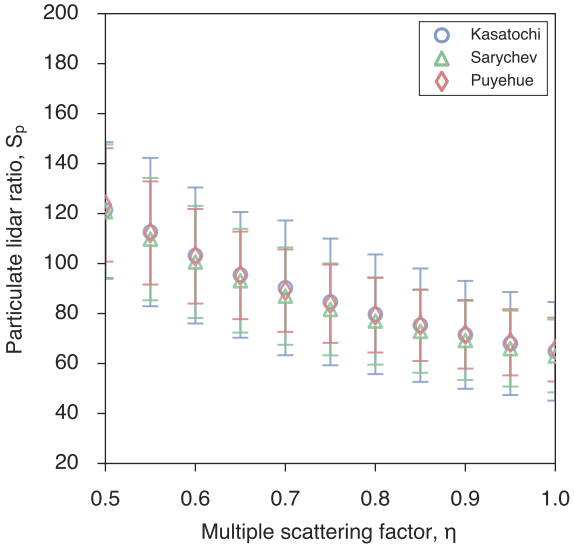

Figure 10. Mean particulate lidar ratios (S_p) for Kasatochi, Sarychev and Puyehue as a function of the multiple scattering factor, η. Error bars represent the standard deviation of S_p for each case study.

Another factor that can contribute to multiple scattering in CALIOP measurements is high depolarisation ($\delta_v > 0.3$). Liu et al. (2011) demonstrated through observations of desert dust that it is the increase in depolarisation ratio with depth into the layer that ultimately determines the magnitude of its multiple scattering effect. For dense desert dust, an increase in depolarisation with depth can lead to a multiple scattering factor of η = 0.75 (Liu et al., 2011). However, for moderately dense layers multiple scattering is expected to be small. Since the volcanic aerosol layers presented here were generally optically thin ($\tau_e <$ 0.8; Fig. 4), the change in depolarisation with layer depth is expected to be small. This argument supports our assumption of minor multiple scattering effects (i.e. η = 0.90–0.95) in the volcanic ash layers considered here.

7 Conclusions

By applying a two-way transmittance constraint to nighttime CALIOP observations, the Fernald solutions were used to derive particulate lidar ratios (S_p) for two classes of volcanic aerosols (fine ash and sulfates). The combination of CALIOP and AIRS measurements has permitted the identification and characterisation of numerous stratospheric volcanic sulfates and fine ash layers produced by three recent eruptions. The mean lidar ratios of the Kasatochi and Sarychev sulfates were found to be 68 $\pm$ 21 sr (median 62 sr) and 66 $\pm$ 15 sr (median 61 sr), respectively. The mean lidar ratios are broadly in agreement with the sulfate lidar ratio of 70 sr of the new stratospheric aerosol scheme (Tackett et al., 2016). However, the lidar ratios of the aged, fine mode ash layers produced by Puyehue were found to be much higher (72 $\pm$ 14 sr; median 70 sr) than the value of 44 sr

Atmos. Chem. Phys. Discuss., doi:10.5194/acp-2016-1173, 2017
Manuscript under review for journal Atmos. Chem. Phys.
Published: 1 February 2017

Atmospheric Chemistry and Physics Discussions

used for volcanic ash. This discrepancy suggests that ash layers could potentially be considered as two subtypes: fine (70 sr) and coarse (44 sr) mode ash.

Errors in the lidar ratio retrieval were most sensitive to errors in the effective two-way particulate transmittance constraint (T_e^2) when layers were optically thin. However, as T_e^2 approaches zero, error in S_p is limited to error in the multiple scattering factor (η) and normalised attenuated backscatter profile ($\beta'_N(r)$). Considering the three main sources of error in the lidar ratio retrieval ($\epsilon(\beta'_N)$, $\epsilon(T_e^2)$ and $\epsilon(\eta)$), a relative error of less than 40% is expected for the particulate lidar ratio retrievals presented here (Fig. 4).

Since the operational lidar ratio retrieval already utilises the two-way transmittance constraint, it is expected that extinction profiles of stratospheric volcanic aerosols could be improved by setting η to a value closer to unity. While 0.6 is a good approximation for cirrus layers (Garnier et al., 2015), an underestimate in multiple scattering translates to an overestimate in the particulate lidar ratio (Fig. 10). Quantification of the multiple scattering factor for volcanic aerosols may further reduce uncertainty in CALIOP derived lidar ratios. This can be achieved, in theory, by comparing visible with infrared optical depth retrievals (e.g. Platt, 1973; Lamquin et al., 2008; Josset et al., 2012; Garnier et al., 2015).

Several differences in the optical properties of the sulfates versus ash were identified through the analysis of layer-integrated optical properties. The low mean layer-integrated volume depolarisation ratios (δ_v) found for Kasatochi and Sarychev indicate that the assumption of collocated SO_2 and $SO_4{}^{2-}$, used to identify sulfate layers, appears to be effective and well-founded for the case studies considered. It was also shown that δ_v can be used to discriminate sulfates from ash particles, and when supplemented with the layer-integrated attenuated colour ratio (χ') these optical properties provide useful information for new stratospheric aerosol classification schemes.

The time evolution of volcanic aerosol optical properties was also investigated. The particulate lidar ratios, for all three case studies, increased with time toward the later stages of aerosol layer development. This can largely be attributed to a decrease in the integrated attenuated backscatter, γ'_p, with time. The δ_v values were consistently low (≤ 0.10) for the Kasatochi sulfate layers and consistently high (~ 0.30) for the Puyehue ash layers. This suggested little change in layer composition with time for the Kasatochi and Puyehue layers. In contrast, an exponential decay (e-folding time of 1 week) in δ_v from 0.25 to 0.05 was observed in the Sarychev layers. A transition from non-spherical to spherical aerosol particles suggested that CALIOP may have captured the formation of sulfate particles as larger irregular particles (ash) were removed. This behaviour was also characterised by a decrease in the layer-integrated attenuated colour ratio with time.

Finally, the methodology presented here was designed to maximise the quality of CALIOP observations of volcanic aerosols. While only stratospheric aerosols were considered, this analysis could be extended to carefully selected observations of tropospheric ash layers. Since the tropospheric ash layers of Eyjafjallajökull were observed by ground-based lidars, this retrieval technique could potentially be validated using coincident CALIOP/AIRS observations.

Acknowledgements. The authors would like to acknowledge Monash University for supporting this research through the Post-graduate Publication Award (PPA). The CALIPSO and AIRS teams are thanked for the provision of the data used in this study. The CALIPSO data

Atmos. Chem. Phys. Discuss., doi:10.5194/acp-2016-1173, 2017
Manuscript under review for journal Atmos. Chem. Phys.
Published: 1 February 2017

were obtained from the NASA Langley Research Center Atmospheric Science Data Center. We also thank Zhaoyan Liu for helpful comments on the manuscript.

Atmos. Chem. Phys. Discuss., doi:10.5194/acp-2016-1173, 2017
Manuscript under review for journal Atmos. Chem. Phys.
Published: 1 February 2017

Atmospheric Chemistry and Physics Discussions

References

Ansmann, A., Tesche, M., Groß, S., Freudenthaler, V., Seifert, P., Hiebsch, A., Schmidt, J., Wandinger, U., Mattis, I., Müller, D., and Wiegner, M.: The 16 April 2010 major volcanic ash plume over central Europe: EARLINET lidar and AERONET photometer observations at Leipzig and Munich, Germany, Geophys. Res. Lett., 37, L13 810, 2010.

Aumann, H. H., Chahine, M. T., Gautier, C., Goldberg, M. D., Kalnay, E., McMillin, L. M., Revercomb, H., Rosenkranz, P. W., Smith, W. L., Staelin, D. H., Strow, L. L., and Susskind, J.: AIRS/AMSU/HSB on the aqua mission: design, science objectives, data products, and processing systems, IEEE Trans. Geosci. Remote Sens., 41, 253–264, 2003.

Bourassa, A. E., Rieger, L. A., Lloyd, N. D., and Degenstein, D. A.: Odin-OSIRIS stratospheric aerosol data product and SAGE III intercomparison, Atmos. Chem. Phys., 12, 605–614, 2012.

Carboni, E., Grainger, R. G., Mather, T. A., Pyle, D. M., Thomas, G. E., Siddans, R., Smith, A. J. A., Dudhia, A., Koukouli, M. E., and Balis, D.: The vertical distribution of volcanic SO_2 plumes measured by IASI, Atmos. Chem. Phys., 16, 4343–4367, 2016.

Carn, S. A., Krotkov, N. A., Yang, K., Hoff, R. M., Prata, A. J., Krueger, A. J., Loughlin, S. C., and Levelt, P. F.: Extended observations of volcanic SO2 and sulfate aerosol in the stratosphere, Atmos. Chem. Phys., 7, 2857–2871, 2007.

Carn, S. A., Clarisse, L., and Prata, A. J.: Multi-decadal satellite measurements of global volcanic degassing, J. Volcanol. Geoth. Res., 311, 99–134, 2016.

Clarisse, L., Coheur, P. F., Prata, F., Hadji-Lazaro, J., Hurtmans, D., and Clerbaux, C.: A unified approach to infrared aerosol remote sensing and type specification, Atmos. Chem. Phys., 13, 2195–2221, 2013.

Cook, C. S., Bethke, G. W., and Conner, W. D.: Remote measurement of smoke plume transmittance using lidar., Appl. Opt., 11, 1742–1748, 1972.

Dutton, E. G. and Christy, J. R.: Solar radiative forcing at selected locations and evidence for global lower tropospheric cooling following the eruptions of El Chichón and Pinatubo, Geophys. Res. Lett., 19, 2313–2316, 1992.

Fernald, F. G.: Analysis of atmospheric lidar observations: some comments., Appl. Opt., 23, 652–652, 1984.

Fernald, F. G., Herman, B. M., and Reagan, J. A.: Determination of Aerosol Height Distributions by Lidar., J. Appl. Meteorol., 11, 482–489, 1972.

Garnier, A., Pelon, J., Vaughan, M. A., Winker, D. M., Trepte, C. R., and Dubuisson, P.: Lidar multiple scattering factors inferred from CALIPSO lidar and IIR retrievals of semi-transparent cirrus cloud optical depths over oceans, Atmos. Meas. Tech., 8, 2759–2774, 2015.

Gerstell, M. F., Crisp, J., and Crisp, D.: Radiative Forcing of the Stratosphere by SO_2 Gas, Silicate Ash, and H_2SO_4 Aerosols Shortly after the 1982 Eruptions of El Chichón., J. Climate, 8, 1060–1070, 1995.

Groß, S., Freudenthaler, V., Wiegner, M., Gasteiger, J., Geiß, A., and Schnell, F.: Dual-wavelength linear depolarization ratio of volcanic aerosols: Lidar measurements of the EyjafjallajOkull plume over Maisach, Germany, Atmos. Environ., 48, 85–96, 2012.

Groß, S., Freudenthaler, V., Wirth, M., and Weinzierl, B.: Towards an aerosol classification scheme for future EarthCARE lidar observations and implications for research needs, Atmos. Sci. Lett., 16, 77–82, 2014.

Hoffmann, A., Ritter, C., Stock, M., Maturilli, M., Eckhardt, S., Herber, A., and Neuber, R.: Lidar measurements of the Kasatochi aerosol plume in August and September 2008 in Ny-Ålesund, Spitsbergen, 115, D00L12, 2010.

Hoffmann, L., Grießbach, S., and Meyer, C. I.: Volcanic emissions from AIRS observations: detection methods, case study, and statistical analysis, Proc. of SPIE, 9242, 924 214, 2014.

Atmos. Chem. Phys. Discuss., doi:10.5194/acp-2016-1173, 2017
Manuscript under review for journal Atmos. Chem. Phys.
Published: 1 February 2017

Holben, B. N., Eck, T. F., Slutsker, I., Tanré, D., and Buis, J. P.: AERONET—A federated instrument network and data archive for aerosol characterization, Remote Sens. Environ., 66, 1–16, 1998.

Hu, Y., Winker, D., Vaughan, M., Lin, B., Omar, A., Trepte, C., Flittner, D., Yang, P., Nasiri, S. L., Baum, B., Holz, R., Sun, W., Liu, Z., Wang, Z., Young, S., Stamnes, K., Huang, J., and Kuehn, R.: CALIPSO/CALIOP Cloud Phase Discrimination Algorithm, J. Atmos. Ocean. Tech., 26, 2293–2309, 2009.

Hughes, I. G. and Hase, T. P. A.: Measurements and their Uncertainties: A Practical Guide to Modern Error Analysis, Oxford University Press, 2010.

Hunt, W. H., Winker, D. M., Vaughan, M. A., Powell, K. A., Lucker, P. L., and Weimer, C.: CALIPSO Lidar Description and Performance Assessment, J. Atmos. Ocean. Tech., 26, 1214–1228, 2009.

Josset, D., Pelon, J., Garnier, A., Hu, Y., Vaughan, M., Zhai, P.-W., Kuehn, R., and Lucker, P.: Cirrus optical depth and lidar ratio retrieval from combined CALIPSO-CloudSat observations using ocean surface echo, J. Geophys. Res., 117, D05 207–14, 2012.

Karagulian, F., Clarisse, L., Clerbaux, C., Prata, A. J., Hurtmans, D., and Coheur, P. F.: Detection of volcanic SO_2, ash, and H_2SO_4 using the Infrared Atmospheric Sounding Interferometer (IASI), J. Geophys. Res. Atmos., 115, D00L02, 2010.

Klüser, L., Erbertseder, T., and Meyer-Arnek, J.: Observation of volcanic ash from Puyehue-Cordón Caulle with IASI, Atmos. Meas. Tech., 6, 35–46, 2013.

Kremser, S., Thomason, L. W., Hobe, M., Hermann, M., Deshler, T., Timmreck, C., Toohey, M., Stenke, A., Schwarz, J. P., Weigel, R., Fueglistaler, S., Prata, F. J., Vernier, J.-P., Schlager, H., Barnes, J. E., Antuña Marrero, J. C., Fairlie, D., Palm, M., Mahieu, E., Notholt, J., Rex, M., Bingen, C., Vanhellemont, F., Bourassa, A., Plane, J. M. C., Klocke, D., Carn, S. A., Clarisse, L., Trickl, T., Neely, R., James, A. D., Rieger, L., Wilson, J. C., and Meland, B.: Stratospheric aerosol—Observations, processes, and impact on climate, Rev. Geophys., 54, 2016.

Kristiansen, N. I., Prata, A. J., and Stohl, A.: Stratospheric volcanic ash emissions from the 13 February 2014 Kelut eruption, Geophys. Res. Lett., 42, 588–596, 2015.

Krotkov, N. A., Schoeberl, M. R., Morris, G. A., Carn, S., and Yang, K.: Dispersion and lifetime of the SO_2 cloud from the August 2008 Kasatochi eruption, J. Geophys. Res. Atmos., 115, D00L20, 2010.

Labitzke, K. and McCormick, M. P.: Stratospheric temperature increases due to Pinatubo aerosols, Geophys. Res. Lett., 19, 207–210, 1992.

Lamquin, N., Stubenrauch, C. J., and Pelon, J.: Upper tropospheric humidity and cirrus geometrical and optical thickness: Relationships inferred from 1 year of collocated AIRS and CALIPSO data, J. Geophys. Res., 113, D00A08–12, 2008.

Lathem, T. L., Kumar, P., Nenes, A., Dufek, J., Sokolik, I. N., Trail, M., and Russell, A.: Hygroscopic properties of volcanic ash, Geophys. Res. Lett., 38, L11 802, 2011.

Liu, Z., Vaughan, M., Winker, D., Kittaka, C., Getzewich, B., Kuehn, R., Omar, A., Powell, K., Trepte, C., and Hostetler, C.: The CALIPSO Lidar Cloud and Aerosol Discrimination: Version 2 Algorithm and Initial Assessment of Performance, J. Atmos. Ocean. Tech., 26, 1198–1213, 2009.

Liu, Z., Winker, D., Omar, A., Vaughan, M., Trepte, C., Hu, Y., Powell, K., Sun, W., and Lin, B.: Effective lidar ratios of dense dust layers over North Africa derived from the CALIOP measurements, J. Quant. Spectrosc. Radiat. Transf., 112, 204–213, 2011.

Mass, C. and Robock, A.: The Short-Term Influence of the Mount St. Helens Volcanic Eruption on Surface Temperature in the Northwest United States, Mon. Weather Rev., 110, 614–622, 1982.

Mattis, I., Ansmann, A., Müller, D., Wandinger, U., and Althausen, D.: Dual-wavelength Raman lidar observations of the extinction-to-backscatter ratio of Saharan dust, Geophys. Res. Lett., 29, 1306–1, 2002.

Mattis, I., Siefert, P., Müller, D., Tesche, M., Hiebsch, A., Kanitz, T., Schmidt, J., Finger, F., Wandinger, U., and Ansmann, A.: Volcanic aerosol layers observed with multiwavelength Raman lidar over central Europe in 2008–2009, J. Geophys. Res., 115, D00L04–9, 2010.

Nakamae, K., Uchino, O., Morino, I., Liley, B., Sakai, T., Nagai, T., and Yokota, T.: Lidar observation of the 2011 Puyehue-Cordón Caulle volcanic aerosols at Lauder, New Zealand, Atmos. Chem. Phys., 14, 12 099–12 108, 2014.

Newhall, C. G. and Self, S.: The volcanic explosivity index (VEI): An estimate of explosive magnitude for historical volcanism, J. Geophys. Res., 87, 1231–1238, 1982.

Niemeier, U., Timmreck, C., Graf, H. F., Kinne, S., Rast, S., and Self, S.: Initial fate of fine ash and sulfur from large volcanic eruptions, Atmos. Chem. Phys., 9, 9043–9057, 2009.

Omar, A., Liu, Z., Vaughan, M., Thornhill, K., Kittaka, C., Ismail, S., Hu, Y., Chen, G., Powell, K., Winker, D., Trepte, C., Winstead, E., and Anderson, B.: Extinction-to-backscatter ratios of Saharan dust layers derived from in situ measurements and CALIPSO overflights during NAMMA, J. Geophys. Res., 115, D24 217–21, 2010.

Omar, A. H., Winker, D. M., Vaughan, M. A., Hu, Y., Trepte, C. R., Ferrare, R. A., Lee, K.-P., Hostetler, C. A., Kittaka, C., Rogers, R. R., Kuehn, R. E., and Liu, Z.: The CALIPSO Automated Aerosol Classification and Lidar Ratio Selection Algorithm, J. Atmos. Ocean. Tech., 26, 1994–2014, 2009.

O'Neill, N. T., Perro, C., Saha, A., Lesins, G., Duck, T. J., Eloranta, E. W., Nott, G. J., Hoffman, A., Karumudi, M. L., Ritter, C., Bourassa, A., Abboud, I., Carn, S. A., and Savastiouk, V.: Properties of Sarychev sulphate aerosols over the Arctic, J. Geophys. Res., 117, D04 203–21, 2012.

Papayannis, A., Mamouri, R. E., Amiridis, V., Giannakaki, E., Veselovskii, I., Kokkalis, P., Tsaknakis, G., Balis, D., Kristiansen, N. I., Stohl, A., Korenskiy, M., Allakhverdiev, K., Huseyinoglu, M. F., and Baykara, T.: Optical properties and vertical extension of aged ash layers over the Eastern Mediterranean as observed by Raman lidars during the Eyjafjallajökull eruption in May 2010, Atmos. Environ., 48, 56–65, 2012.

Pitts, M. C., Poole, L. R., and Thomason, L. W.: CALIPSO polar stratospheric cloud observations: second-generation detection algorithm and composition discrimination, Atmos. Chem. Phys., 9, 7577–7589, 2009.

Platt, C.: Lidar and Radiometric Observations of Cirrus Clouds, J. Atmos. Sci., 30, 1191–1204, 1973.

Povey, A. C., Grainger, R. G., Peters, D. M., and Agnew, J. L.: Retrieval of aerosol backscatter, extinction, and lidar ratio from Raman lidar with optimal estimation, Atmos. Meas. Tech., 7, 757–776, 2014.

Prata, A. J. and Prata, A. T.: Eyjafjallajökull volcanic ash concentrations determined using Spin Enhanced Visible and Infrared Imager measurements, J. Geophys. Res. Atmos., 117, D00U23, 2012.

Prata, A. T.: Remote sensing of volcanic eruptions: from aviation hazards to global cooling, in: Plate Boundaries and Natural Hazards, edited by Duarte, J. C. and Schellart, W. P., 2016.

Prata, A. T., Siems, S. T., and Manton, M. J.: Quantification of volcanic cloud top heights and thicknesses using A-train observations for the 2008 Chaitén eruption, J. Geophys. Res. Atmos., 120, 2928–2950, 2015.

Ridley, D. A., Solomon, S., Barnes, J. E., Burlakov, V. D., Deshler, T., Dolgii, S. I., Herber, A. B., Nagai, T., Neely, R. R., Nevzorov, A. V., Ritter, C., Sakai, T., Santer, B. D., Sato, M., Schmidt, A., Uchino, O., and Vernier, J. P.: Total volcanic stratospheric aerosol optical depths and implications for global climate change, Geophys. Res. Lett., 41, 7763–7769, 2014.

Rieger, L. A., Bourassa, A. E., and Degenstein, D. A.: Merging the OSIRIS and SAGE II stratospheric aerosol records, J. Geophys. Res. Atmos., 120, 8890–8904, 2015.

Atmos. Chem. Phys. Discuss., doi:10.5194/acp-2016-1173, 2017
Manuscript under review for journal Atmos. Chem. Phys.
Published: 1 February 2017

Rienecker, M. M., Suarez, M. J., Todling, R., Bacmeister, J., Takacs, L., Liu, H. C., Gu, W., Sienkiewicz, M., Koster, R. D., Gelaro, R., Stajner, I., and Nielsen, J. E.: The GEOS-5 Data Assimilation System— Documentation of Versions 5.0.1, 5.1.0, and 5.2.0, Technical Report Series on Global Modeling and Data Assimilation, 27, NASA/TM-2008-104606, 1–118, 2008.

Rogers, R. R., Hostetler, C. A., Hair, J. W., Ferrare, R. A., Liu, Z., Obland, M. D., Harper, D. B., Cook, A. L., Powell, K. A., Vaughan, M. A., and Winker, D. M.: Assessment of the CALIPSO Lidar 532 nm attenuated backscatter calibration using the NASA LaRC airborne High Spectral Resolution Lidar, Atmos. Chem. Phys., 11, 1295–1311, 2011.

Rybin, A., Chibisova, M., Webley, P., Steensen, T., Izbekov, P., Neal, C., and Realmuto, V.: Satellite and ground observations of the June 2009 eruption of Sarychev Peak volcano, Matua Island, Central Kuriles, Bull. Volcanol., 73, 1377–1392, 2011.

Santer, B. D., Bonfils, C., Painter, J. F., Zelinka, M. D., Mears, C., Solomon, S., Schmidt, G. A., Fyfe, J. C., Cole, J. N. S., Nazarenko, L., Taylor, K. E., and Wentz, F. J.: Volcanic contribution to decadal changes in tropospheric temperature, Nat. Geosci., 7, 185–189, 2014.

Sassen, K. and Cho, B. S.: Subvisual-Thin Cirrus Lidar Dataset for Satellite Verification and Climatological Research., J. Appl. Meteorol., 31, 1275–1285, 1992.

Sato, M., Hansen, J. E., McCormick, M. P., and Pollack, J. B.: Stratospheric Aerosol Optical Depths, 1850–1990, J. Geophys. Res., 98, 22 987, 1993.

Sawamura, P., Vernier, J. P., Barnes, J. E., Berkoff, T. A., Welton, E. J., Alados-Arboledas, L., Navas-Guzmán, F., Pappalardo, G., Mona, L., Madonna, F., Lange, D., Sicard, M., Godin-Beekmann, S., Payen, G., Wang, Z., Hu, S., Tripathi, S. N., Cordoba-Jabonero, C., and Hoff, R. M.: Stratospheric AOD after the 2011 eruption of Nabro volcano measured by lidars over the Northern Hemisphere, Environ. Res. Lett., 7, 034 013, 2012.

Solomon, S., Daniel, J. S., Neely, R. R., Vernier, J. P., Dutton, E. G., and Thomason, L. W.: The persistently variable "background" stratospheric aerosol layer and global climate change., Science, 333, 866–870, 2011.

Stephens, G. L., Vane, D. G., Boain, R. J., Mace, G. G., Sassen, K., Wang, Z., Illingworth, A. J., O'Connor, E. J., Rossow, W. B., Durden, S. L., Miller, S. D., Austin, R. T., Benedetti, A., Mitrescu, C., and CloudSat Science Team, T.: The CloudSat mission and the A-Train: A new dimension of space-based observations of clouds and precipitation, B. Am. Meteorol. Soc., 83, 1771–1790, 2002.

Tackett, J. L., Omar, A. H., Vaughan, M. A., Kar, J., Trepte, C. R., Winker, D. M., and Magill, B.: New Stratospheric Aerosol Subtypes Implemented in CALIOP Version 4 Level 2, in: CALIPSO/CloudSat Science Team Meeting. 1-3 March 2016., 2016.

Theys, N., De Smedt, I., Van Roozendael, M., Froidevaux, L., Clarisse, L., and Hendrick, F.: First satellite detection of volcanic OClO after the eruption of Puyehue-Cordón Caulle, Geophys. Res. Lett., 41, 667–672, 2014.

Thomason, L. W. and Pitts, M. C.: CALIPSO observations of volcanic aerosol in the stratosphere, Proc. SPIE, 7153, 71 530O–1–71 530O–8, 2008.

Vaughan, M. A., Winker, D. M., and Powell, K. A.: CALIOP Algorithm Theoretical Basis Document Part 2: Feature Detection and Layer Properties Algorithms [Available online at http://www-calipso.larc.nasa.gov/resources/pdfs/PC-SCI-202_Part2_rev1x01.pdf], 2005.

Vaughan, M. A., Powell, K. A., Kuehn, R. E., Young, S. A., Winker, D. M., Hostetler, C. A., Hunt, W. H., Liu, Z., McGill, M. J., and Getzewich, B. J.: Fully Automated Detection of Cloud and Aerosol Layers in the CALIPSO Lidar Measurements, J. Atmos. Ocean. Tech., 26, 2034–2050, 2009.

Vernier, J. P., Pommereau, J. P., Garnier, A., Pelon, J., Larsen, N., Nielsen, J., Christensen, T., Cairo, F., Thomason, L. W., Leblanc, T., and McDermid, I. S.: Tropical stratospheric aerosol layer from CALIPSO lidar observations, 114, D00H10, 2009.

Vernier, J. P., Thomason, L. W., Pommereau, J. P., Bourassa, A., Pelon, J., Garnier, A., Hauchecorne, A., Blanot, L., Trepte, C., Degenstein, D., and Vargas, F.: Major influence of tropical volcanic eruptions on the stratospheric aerosol layer during the last decade, Geophys. Res. Lett., 38, L12 807, 2011.

Vernier, J. P., Fairlie, T. D., Murray, J. J., Tupper, A., Trepte, C., Winker, D., Pelon, J., Garnier, A., Jumelet, J., Pavolonis, M., Omar, A. H., and Powell, K. A.: An Advanced System to Monitor the 3D Structure of Diffuse Volcanic Ash Clouds, J. Appl. Meteorol. Climatol., 52, 2125–2138, 2013.

Wang, X., Boselli, A., D'Avino, L., Pisani, G., Spinelli, N., Amodeo, A., Chaikovsky, A., Wiegner, M., Nickovic, S., Papayannis, A., Perrone, M. R., Rizi, V., Sauvage, L., and Stohl, A.: Volcanic dust characterization by EARLINET during Etna's eruptions in 2001–2002, Atmos. Environ., 42, 893–905, 2008.

Waythomas, C. F., Scott, W. E., Prejean, S. G., Schneider, D. J., Izbekov, P., and Nye, C. J.: The 7–8 August 2008 eruption of Kasatochi Volcano, central Aleutian Islands, Alaska, J. Geophys. Res., 115, B00B06–23, 2010.

Wiegner, M., Gasteiger, J., Groß, S., Schnell, F., Freudenthaler, V., and Forkel, R.: Characterization of the Eyjafjallajökull ash-plume: Potential of lidar remote sensing, Phys. Chem. Earth, 45-46, 79–86, 2012.

Williams, D. B. and Thomas, H. E.: An assessment of volcanic hazards to aviation – a case study from the 2009 Sarychev Peak eruption, Geomat. Nat. Haz. Risk., 2, 233–246, 2011.

Winker, D. M.: Accounting for multiple scattering in retrievals from space lidar, in: Proc. SPIE, pp. 128–139, NASA Langley Research Ctr., USA, 2003.

Winker, D. M. and Osborn, M. T.: Airborne Lidar Observations of the Pinatubo Volcanic Plume, Geophys. Res. Lett., 19, 167–170, 1992a.

Winker, D. M. and Osborn, M. T.: Preliminary analysis of observations of the Pinatubo volcanic plume with a polarization-sensitive lidar, Geophys. Res. Lett., 19, 171–174, 1992b.

Winker, D. M., Pelon, J., Coakley Jr., J. A., Ackerman, S. A., Charlson, R. J., Colarco, P. R., Flamant, P., Fu, Q., Hoff, R. M., Kittaka, C., Kubar, T. L., Le Treut, H., McCormick, M. P., MéGie, G., Poole, L., Powell, K., Trepte, C., Vaughan, M. A., and Wielicki, B. A.: The CALIPSO Mission: A Global 3D View of Aerosols and Clouds, B. Am. Meteorol. Soc., 91, 1211–1229, 2010.

Winker, D. M., Liu, Z., Omar, A., Tackett, J., and Fairlie, D.: CALIOP observations of the transport of ash from the Eyjafjallajökull volcano in April 2010, J. Geophys. Res., 117, D00U15, 2012.

Young, S. A.: Analysis of lidar backscatter profiles in optically thin clouds., Appl. Opt., 34, 7019–7031, 1995.

Young, S. A. and Vaughan, M. A.: The Retrieval of Profiles of Particulate Extinction from Cloud-Aerosol Lidar Infrared Pathfinder Satellite Observations (CALIPSO) Data: Algorithm Description, J. Atmos. Ocean. Tech., 26, 1105–1119, 2009.

Young, S. A., Winker, D. M., Vaughan, M. A., Hu, Y., and Kuehn, R. E.: CALIOP Algorithm Theoretical Basis Document Part 4: Extinction Retrieval Algorithms [Available online at http://www-calipso.larc.nasa.gov/resources/pdfs/PC-SCI-202_Part4_v1.0.pdf], 2008.

Young, S. A., Vaughan, M. A., Kuehn, R. E., and Winker, D. M.: The Retrieval of Profiles of Particulate Extinction from Cloud–Aerosol Lidar and Infrared Pathfinder Satellite Observations (CALIPSO) Data: Uncertainty and Error Sensitivity Analyses, J. Atmos. Ocean. Tech., 30, 395–428, 2013.